SCALABLE CORROSION RESISTANT COATINGS FOR THERMAL APPLICATIONS

BY

SIAVASH KHODAKARAMI

THESIS

Submitted in partial fulfillment of the requirements
for the degree of Master of Science in Mechanical Engineering
in the Graduate College of the
University of Illinois at Urbana-Champaign, 2021

Urbana, Illinois

Adviser:

Professor Nenad Miljkovic

ABSTRACT

Corrosion of metallic substrates is a problem for a variety of applications. Corrosion can be mitigated with the use of an electrically insulating coating protecting the substrate. Thick millimetric coatings, such as paints, are generally more corrosion resistant when compared to nanoscale coatings. However, for thermal systems, thick coatings are undesirable due to the resulting decrease in overall heat transfer stemming from the added coating thermal resistance. Hence, the development of ultra-thin (< 10 μm) coatings is of great interest. Ultra-thin inorganic silicon dioxide (SiO_2) coatings applied by sol-gel chemistries or chemical vapor deposition, as well as organic coatings such as Parylene C have great anti-corrosion performance due to their high dielectric breakdown and low moisture permeability. However, their application to arbitrarily shaped metals is difficult or expensive. Here, we develop a sol-gel solution capable of facile and controllable dip coating on arbitrary metals, resulting in a very smooth (< 5 nm roughness), thin (~ 3 μm), and conformal coating of dense SiO_2. To benchmark our material, we compared the corrosion performance with in-house synthesized superhydrophobic aluminum and copper samples, Parylene C coated substrates, and smooth hydrophobic surfaces functionalized with a hydrophobic self-assembled monolayer. To comparison with state-of-the-art commercial coatings, copper substrates were coated with an organo-ceramic SiO_2 layer created by an elevated temperature and atmospheric pressure metal organic chemical vapor deposition process (AP MO-CVD). To characterize corrosion performance, we electrochemically investigated the corrosion resistance of all samples through potentiodynamic polarization studies and electrochemical impedance spectroscopy. To benchmark the coating durability as well as to demonstrate scalability, we tested internally coated copper tubes in a custom-built corrosion flow loop to simulate realistic working conditions with shear and particulate saltwater flow. The sol-

gel and Parylene C coatings demonstrated a 95% decrease in corrosion rate during electrochemical tests. Copper tube weight loss was reduced by 75% for the sol-gel SiO_2-coated tubes when sea water was used as the corrosive fluid in the test loop. This work not only demonstrates scalable coating methodologies for applying ultra-thin anti-corrosion coatings, it develops mechanistic understanding of corrosion mechanisms on a variety of functional surfaces and substrates.

TABLE OF CONTENTS

CHAPTER 1: INTRODUCTION

Corrosion is a major problem for a variety of applications. The economic impact of corrosion is estimated to be up to 5% of the global gross national product.[1] In thermal systems, corrosion inside of tubes and channels decreases heat transfer, increase nucleation site density for heterogeneous scale formation, acts as a fouling product via corrosion fouling, and increases pressure drop. Hence, corrosion results in lower system efficiency and eventually reduction in lifespan.[2] To combat corrosion, corrosion prevention coatings have been developed. One of the most common anti-corrosion coating formulations in the heat exchanger sector is an *e-coat* of an epoxy-based chemistry to deposit a thick corrosion protection layers on arbitrarily shaped metals. Although successful at preventing corrosion, *e-coat* formulations represent an expensive and time-consuming solution that is particularly well suited for heat transfer applications having characteristically low heat transfer rates (coefficients) such as those used in air-side applications. Furthermore, the need for surface pre-treatment (*e.g.* with zinc phosphate) and a topcoat of paint to prevent epoxy *e-coat* failure against ultraviolet degradation, makes the added cost of the *e-coat* process prohibitive for many applications. To enable greater scalability for a variety of systems, as well as to reduce cost, great attention has been given to sol-gel coatings of silicon dioxide (SiO_2) as a replacement for *e-coat*.[3-5] The sol-gel SiO_2 deposition possesses many advantages, such as an eco-friendly chemistry, great stability, and deposition capability at relatively low temperatures (room temperature). The low temperature and atmospheric pressure sol-gel process makes it particularly advantageous when compared to conventional chemical vapor deposition (CVD) of SiO_2 which typically requires well controlled environments with temperatures approaching 800ºC, which can affect the metallurgy of the substrate. Although atmospheric pressure metal organic chemical vapor deposition (AP MO-CVD) enables the reduction of deposition temperatures to

300°C, which is compatible with copper (Cu) alloy substrates, room temperature sol-gel remains preferred due to increased flexibility in terms of substrate material. Furthermore, sol-gel coatings have been shown to be good alternatives to hazardous and carcinogenic chromate coatings for metallic substrates,[4, 6] and finite-lifetime sacrificial coatings which use another metal with lower electrode potential to keep the underlying substrate corrosion free by sacrificing itself.[7-8] Recently, there has been a great interest in developing hybrid sol-gel coatings. Hybrid inorganic-organic sol-gel coatings were established by attaching titanium or zirconium alkoxides to the silica matrix and it was shown to have improved adhesion, specifically on Magnesium substrate.[9] Recently, intrinsically healable polymers that use reversible covalent bonds have been used in the sol-gel formulations to improve the long-term barrier properties in.[1] Functional sol-gel based coating with improved wettability, transparency, and abrasion resistance, in addition to anti-corrosion properties, are a developing field of research.[10] In addition to solid coatings, studies have shown rough superhydrophobic surfaces to have good corrosion resistance.[11-13] Superhydrophobicity is achieved when a textured surface is combined with a low surface energy chemistry leading to apparent water contact angles greater than 150° and contact angle hysteresis lower than 10°.[14-15] When the electrolyte contacts the superhydrophobic substrate, air is trapped in the micro and nanostructures between the low surface energy substrate and the liquid. The trapped air act as a barrier, preventing the corrosive species from attacking the substrate.[16] Although past sol-gel and structured superhydrophobic coatings have successfully prevented corrosion of metal substrates, they suffer from poor reliability,[17-18] poor ability to scale to arbitrary surfaces, and a lack of control of their thickness such that the coating does not become an impedance to heat transfer.

Here, we develop a sol-gel-based dip coating manufacturing methodology to deposit thin (< 10 μm) SiO_2 corrosion barrier films on arbitrary shaped surfaces composed of arbitrary metals.

By controlling the velocity of the dip coating process, we vary the coating thicknesses without changing the sol-gel chemistry. To benchmark corrosion performance of our coating with well-established formulations, we also fabricated superhydrophobic, solid polymeric, solid slippery, and monolayer hydrophobic coatings on Cu and aluminum (Al) substrates. The corrosion resistance and mechanism governing corrosion on each coating was quantitatively measured by potentiodynamic curves as well as electrochemical impedance spectroscopy. To better understand durability and emulate realistic flow corrosion conditions, we built a custom flow loop to study the anti-corrosion performance and durability of coated Cu tubes with salt water flow both at room temperature and at 40°C in a laminar regime with Reynolds number ≈ 600. The flow corrosion experiments not only quantifiably estimate coating durability and performance, they provide a platform to estimate the ease of scalable implementation in hard-to-reach internal geometries. Lastly, we characterize all coatings using aggressive salt corrosion conditions in a salt-spray chamber to identify durability of the coating formulations. Our work not only demonstrates an ultra-scalable sol-gel coating for corrosion protection, it develops mechanistic understanding of corrosion on a variety of thin functional coatings deposited on Cu and Al substrates.

CHAPTER 2: COATING PREPARATION

Copper and Aluminum Sample Preparation: Polished copper (Cu) and aluminum (Al) (Mirror-like 110 Copper and 6061 Aluminum, McMaster) were purchased and cut into 2.5 cm × 7.6 cm × 0.16 cm sizes. Then the Cu and Al tabs were degreased using commercial degreaser (Orange Blast, Greased Lightning) and rinsed with deionized (DI) water, followed by isopropanol (CAS #: 67-63-0, Sigma Aldrich) and finally dried with a clean nitrogen gas flow. After cleaning, the tabs were sonicated in acetone (CAS #: 67-64-1, Sigma Aldrich) for 5 minutes. After sonication, the tabs were sequentially rinsed with acetone, isopropanol, DI water and again isopropanol followed by air drying. For tube samples (3/16" diameter Cu tubes, McMaster), the tubes were cut to be approximately 25 cm in length with the same cleaning process done prior to coating.

Sol-Gel Solution and Coating Method: To prepare the sol-gel solution, Tetraethyl orthosilicate (TEOS, CAS #: 78-10-4, Sigma Aldrich) and Trimethoxymethylsilane (MTMS, CAS #: 1185-55-3, Sigma Aldrich) were mixed in a glass beaker in a 1:2.5 molar ratio. The beaker was placed in an ice bath and stirred for 5 minutes using a magnetic stirrer (Fig. 1). Sodium hydroxide (CAS #: 1310-73-2) was mixed with DI water to adjust the PH of the resultant solution to 14.5 and it was added as a catalyst to the silane solution with continual stirring. Ethanol (CAS #: 64-17-5, Sigma Aldrich) was added as the solvent and stirring continued for another 10 minutes. The molar ratio of TEOS:MTMS:DI:ethanol was 1:2.5:4.1:3. The solution was kept in an ice bath throughout the dip coating method. The good corrosion resistance of the sol-gel depends on a good bonding of Si-O group to the surface of the metal. Bonding of the silanol groups to Cu substrate can be difficult.[19-20] However, with the right chemistry, it is possible to achieve strong bonding, enough for corrosion protection.[21] The Cu and Al samples were coated immediately after the cleaning process to eliminate hydrocarbon adsorption from the ambient.[22-23] The samples were held by a

clamp and vertical motion was controlled by a dc motor (Fig. 1). The velocity of the dip coating was controlled by the applied voltage to the dc motor. The thickness of the coating was adjusted by changing the sample withdrawal velocity. For our case, the withdrawal velocity was kept at 17.1 cm/min to obtain a constant coating thickness for all samples. The thickness was measured to be 3 ± 0.1 μm using ellipsometry (J.A. Woollam VASE). After sol-gel coating, the samples were left to dry at room temperature for 10 minutes and then were further heat treated at 500°C for 30 minutes in a nitrogen furnace (Lindberg 2" tube furnace) in order to ensure sintering and densification of the SiO_2 coating.[21] Based on the thermal applications (heat exchangers) that the coating is developed for, the coating was applied on flat samples for electrochemical characterization and also tube internal surfaces to allow us the evaluation of the coating performance in flow corrosion condition.

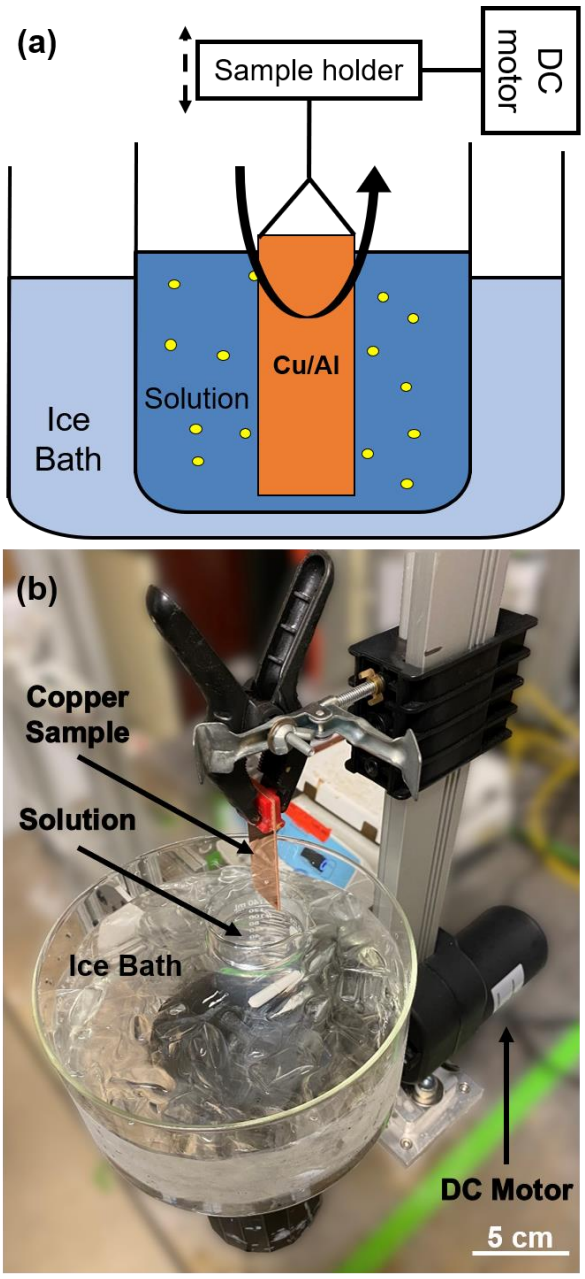

Figure 1. (a) Schematic and (b) photograph of the dip coating apparatus. The sol-gel solution was kept in the ice bath to maintain the solution temperature. A dc motor was used to control the sample withdrawal speed. Schematic not to scale.

SOCAL Coating: To provide a benchmark and to study the effect of surface energy on corrosion, we applied a slippery omniphobic covalently attached liquid (SOCAL) on top of the sol-gel coated Cu and Al samples.[24] Due to the low concentration of hydroxyl groups on Cu and Al substrates, direct deposition of SOCAL was unsuccessful. Therefore the SOCAL was coated on top of the sol-gel coating with SiO_2 acting as an intermediate layer between the substrate and SOCAL.[21, 25-26] The detailed process of SOCAL development is explained elsewhere.[21, 24] Briefly, we started by making a 100:10:1 wt% mixture of isopropanol: Dimethyldimethoxysilane (DMDMS, CAS#: 1112-39-6, Sigma-Aldrich): sulfuric acid (CAS#: 7664-93-9, Sigma-Aldrich). After stirring the solution for 30 seconds, the mixture was left to rest in a sealed glass container for 20 minutes at room temperature. The sol-gel coated Cu and Al samples were soaked in diluted sulfuric acid (2%) to remove any residuals on the surface prior to coating with SOCAL. Then the sample was dipped into the SOCAL solution and removed slowly by hand and left to dry at room temperature for 20 minutes. Just after drying, the sample was rinsed in sequence with DI water, isopropanol, toluene (CAS #: 108-88-3, Sigma Aldrich) and isopropanol followed by nitrogen gas drying.

Hydrophobic and Superhydrophobic Coatings: The superhydrophobic (SHP) Al tabs were fabricated using the processes described in previous literature.[27-29] First, samples were sonicated in acetone for 5 minutes followed by rinsing with isopropanol and DI water and drying with dry nitrogen gas. Then, the Al sample was immersed in 2M hydrochloric acid for 5 minutes to form microstructures on the surface and subsequently immersed in a 90°C DI water bath to create nanostructured boehmite on top of the microstructures. To functionalize the surface, a very thin (~3 nm) layer of Heptadecafluoro-1,1,2,2-tetrahydrodecyl trimethoxysilane (HTMS) was deposited on the surface by atmospheric pressure CVD. To achieve HTMS deposition, 5% v/v

HTMS was mixed with toluene and placed in a clean glass container. The mixture container was then placed in a larger glass container along with the Al tabs placed adjacent to the HTMS mixture container, and the larger container sealed using an Al foil lid. Then the large glass container was placed in an atmospheric pressure oven (Lindberg Blue M, Thermo Scientific) at 85°C for 3 hours.

The superhydrophobic Cu tabs were fabricated based on a previously developed procedure.[30-31] The pre-cut Cu samples were sonicated in acetone for 5 minutes followed by rinsing with isopropanol and DI water and drying with a dry nitrogen gas stream. Next, the samples were immersed in a 2M hydrochloric acid solution for 30 seconds and rinsed with DI water and dried with a dry nitrogen gas steam. Subsequently, the sample was immersed in an alkaline solution composed of sodium chlorite, sodium hydroxide and sodium phosphate at 95°C for 5 minutes to create the copper oxide (CuO) structures.[30] Functionalization of the surface was done with HTMS using the same procedure as described for the Al superhydrophobic samples.

In addition to rough superhydrophobic samples, smooth hydrophobic Cu and Al tabs were fabricated by deposition of HTMS on cleaned samples without micro/nanostructures. The smooth hydrophobic samples were created in order to allow for a comparison between hydrophobic and superhydrophobic Cu and Al surfaces and to study the effect of air pockets in the superhydrophobic state on corrosion mechanisms.

To obtain a benchmark comparison with thicker and more durable coating formulations, we fabricated smooth Al and Cu substrates coated with Parylene C. Parylene C was specifically chosen due to its good corrosive protection capability and high dielectric strength[32] as well as low water permeability, good durability, and hydrophobicity.[33] The basic monomer of Parylene is poly(para-xylylene), a completely linear, highly crystalline material. Parylene C is made by modification of the monomer by the substitution of a chlorine atom for one of the aromatic

hydrogens. In order to obtain a conformal coating, Parylene C was deposited on the samples by CVD using a Specialty Coating Systems Labcoater 2 Parylene deposition system. The Parylene C thickness was 3 μm to provide an identical coating thickness as the sol-gel coating.

CHAPTER 3: SURFACE CHARACTERIZATION

Contact Angle Measurement: Contact angle measurements were carried out using microgoniometry (MCA 3, Kyowa Interface Science). The apparent advancing contact angle (θ_a), apparent receding contact angle (θ_r) and contact angle hysteresis ($\Delta\theta = \theta_a - \theta_r$) were measured on four different spots for each sample and averaging done to gain understanding of measurement uncertainty and standard deviation. Note, measurement uncertainty may be larger than the reported standard deviation of the multiple measurements in Table 1.[34] The measurement uncertainty is approximately 2° and 5° for hydrophobic and superhydrophobic surfaces, respectively. All contact angle data were analyzed using the image processing software (FAMAS, Interface Measurement and Analysis System) with the circle fitting method.

Table 1. Contact angle measurement results of DI water droplets at room temperature. Measurements were done using a microgoniometer on 4 different spots for each sample (see Methods). The ± values represent standard deviation between the multiple spatial measurements.

Substrate	Coating	Coating Thickness	θ_a [°]	θ_r [°]	$\Delta\theta$ [°]
Polished Al	Uncoated	-	89 ± 1	30 ± 1	59 ± 1
	HTMS	< 3 nm	111 ± 2	68 ± 3	43 ± 3
	SHP	Structure < 400 nm	162 ± 3	161 ± 3	2 ± 4
		Functional group < 3 nm			
	Sol-gel	< 3 μm	110 ± 1	83 ± 2	27 ± 2
	Sol-gel+SOCAL	< 3 μm	112 ± 1	92 ± 1	19 ± 1
	Parylene C	3 μm	92 ± 1	76 ± 2	15 ± 2
	AP MO-CVD SiO_2	400 nm	82 ± 1	62 ± 2	20 ± 2
Polished Cu	Uncoated	-	83 ± 1	23 ± 4	61 ± 4
	HTMS	< 3 nm	118 ± 1	78 ± 1	40 ± 2
	SHP	Structure < 2 μm	166 ± 1	164 ± 1	2 ± 1
		Functional group < 3 nm			

Table 1. (Cont.)

	Sol-gel	< 3 μm	106 ± 3	86 ± 3	20 ± 4
	Sol-gel+SOCAL	< 3 μm	112 ± 1	97 ± 3	15 ± 3
	Parylene C	3 μm	91 ± 1	75 ± 2	17 ± 2
	AP MO-CVD SiO_2	400 nm	81 ± 1	61 ± 1	20 ± 1

Scanning Electron Microscopy (SEM): The SEM images of the polished Cu and Al substrates coated with sol-gel, Parylene C, and superhydrophobic coatings were taken on a Hitachi S-4700 at accelerating voltage of 10 kV and emission current of 10 μA. Except for the bare Cu, all other coatings were either electrically insulating (sol-gel and Parylene C) or had low electrical conductivity (superhydrophobic samples). Therefore, a thin gold (Au) layer (< 10 nm) was sputtered on the samples using an Au sputter coater (Emitech K575) prior to taking SEM images to avoid charging. All images were taken in the ultra-high-resolution mode with a working distance of 6 mm.

As shown in Figure 2, the sol-gel and Parylene C coatings filled imperfections and reduced the roughness of the Cu substrate. However, some pinholes were observable on the sol- gel coating. The pinholes were likely locations for corrosion initiation and coating delamination. For better quantification of the pinholes, the 50 k and 200 k magnified SEM images of the sol-gel surface are shown in Figure 3.

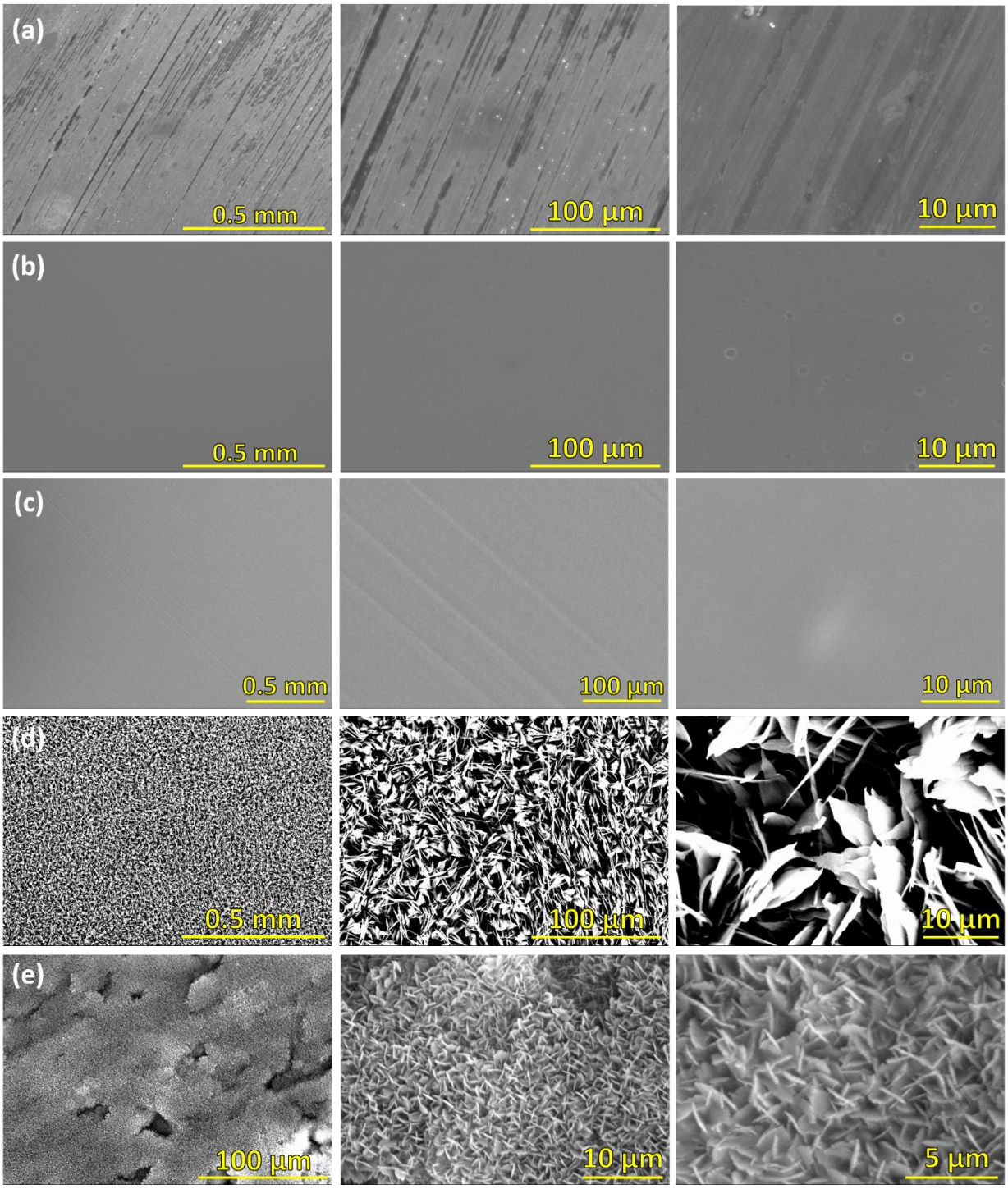

Figure 2. Top-view SEM images of (a) uncoated polished Cu, (b) sol-gel coated Cu, (c) Parylene C coated Cu, (d) superhydrophobic Cu and (e) superhydrophobic Al. The vertical marks in (a) stem from milling marks during Cu manufacture that could not be removed during polishing.

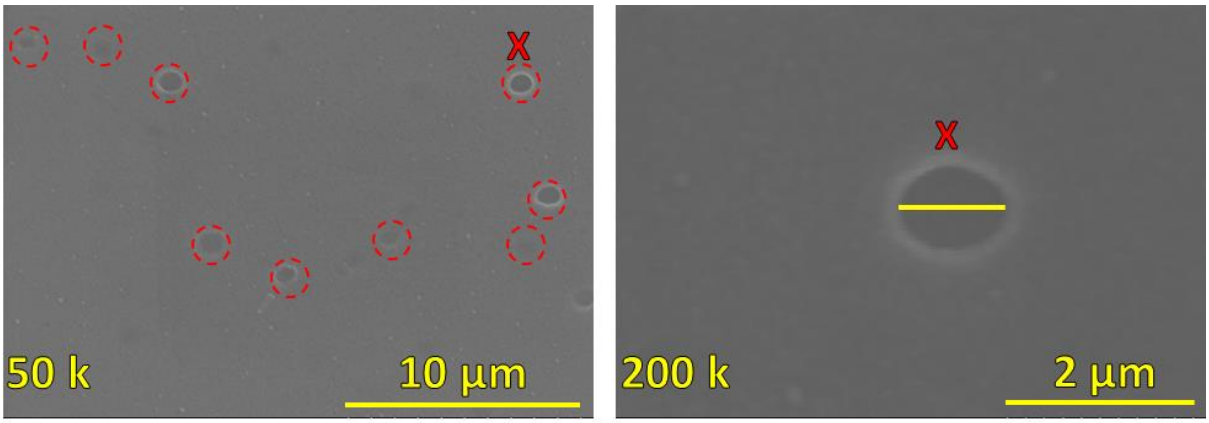

Figure 3. SEM image of the Cu sample coated with sol-gel at low (50k, left) and high (200k, right) magnification. The estimated pinhole diameter was observed to be as high as 1.1 µm. The red dashed circles on the left image identify larger pinholes for clarity.

Atomic Force Microscopy (AFM): To better quantify the topography of the samples, AFM was conducted on an Asylum Research MFP- 3D system. Tapping mode was used to scan a 15 µm × 15 µm randomly chosen area near the center of each sample. A Tap300 (Ted Pella) AFM tip was used and the scanning frequency was set to 0.8 Hz for all measurements. The drive amplitude was varied (100 mV – 350 mV) to get the best possible scanning with a low noise in phase angle. Open source Gwyddion software was used for image processing.[35]

Figure 4 shows AFM scans of all samples. Since the coating topology was the same on both polished Cu and Al substrates shown through SEM, AFM was done only on Cu substrates for coatings with differing AFM scans conducted for the boehmite nanostructures and CuO microstructures. The root mean squared roughness (S_q) of the polished Cu was measured to be 24 nm. By using the conformal Parylene C coating, S_q was reduced to 7 nm. Interestingly, S_q was even smaller for the sol-gel and SOCAL coating, reaching S_q = 3 nm. The low roughness represents a smooth surface with low nucleation site density that, along with its intrinsic hydrophobicity, is capable of reducing scaling. As expected, S_q was higher on the CuO and boehmite structures, with S_q = 273 nm and 164 nm, respectively. The S_q of the Cu with AP MO-

CVD SiO_2 coating is higher than the uncoated polished Cu. This is due to the necessary pickling pretreatment step prior to the CVD process which will increase the roughness of the surface. Therefore, despite of the pinhole free coating achieved by the high temperature AP MO-CVD process, the roughness is high enough to manifest a relatively high droplet adhesion to the surface.

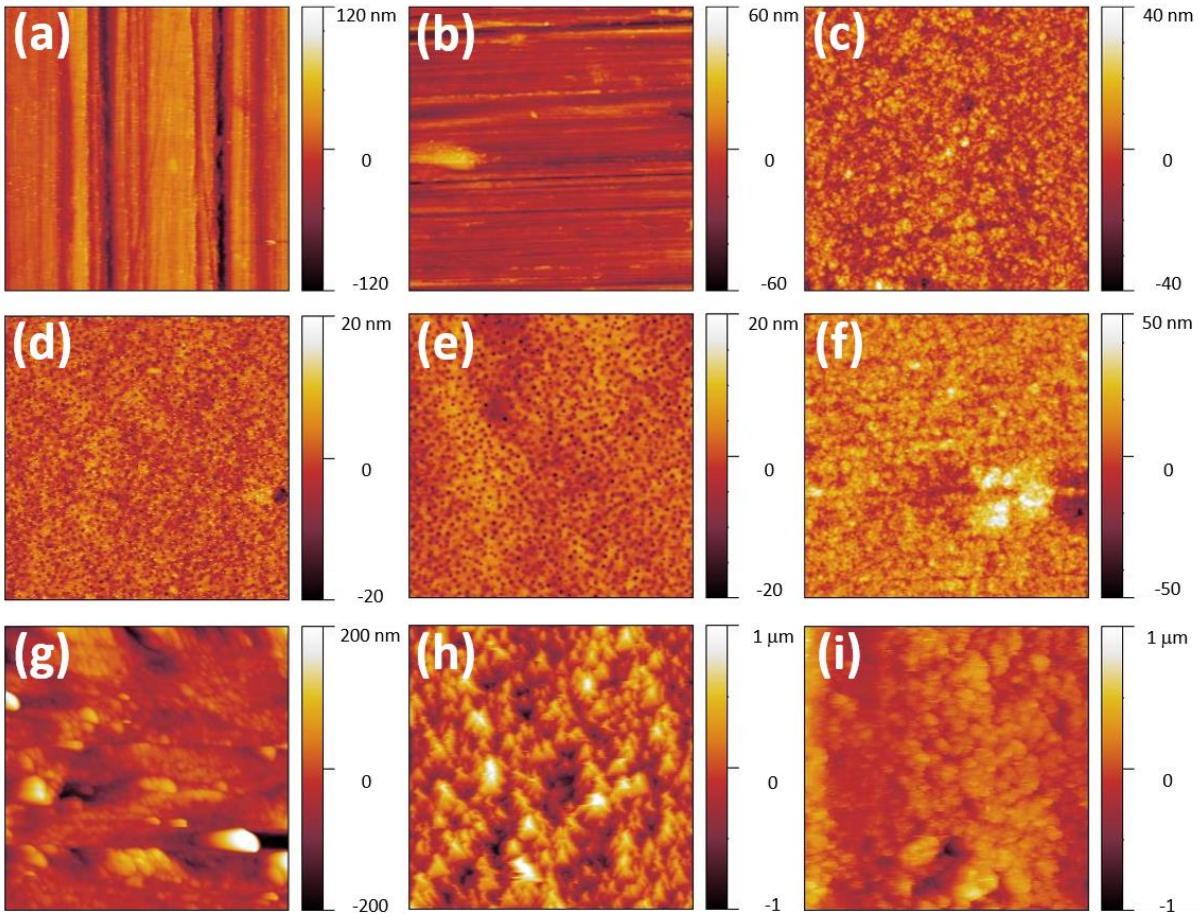

Figure 4. AFM scans of (a) unmodified polished Cu (0° Scan) (S_q = 24 nm), (b) unmodified polished Al (90° Scan) (S_q = 10 nm), (c) Parylene C coated polished Cu (S_q = 7 nm), (d) sol-gel coated polished Cu (S_q = 3 nm), (e) sol-gel-SOCAL coated polished Cu (S_q = 3 nm), (f) un-sintered sol-gel coated polished Cu (S_q = 9 nm), (g) AP MO-CVD SiO_2 on polished Cu (S_q = 34 nm) (h) CuO grown on polished Cu (S_q = 273 nm), and (i) boehmite grown on polished Al (S_q = 164 nm). The scan area for each image is 15 µm × 15 µm.

CHAPTER 4: ELECTROCHEMICAL MEASUREMENTS

Potentiodynamic Polarization: Polarization curves for Al and Cu substrates with different coatings are shown in Figure 5. The anodic reaction for corrosion of Cu in NaCl solution and cathodic reaction for oxygen reduction is as follows:[36]

$$\mathrm{Cu} \rightarrow \mathrm{Cu}^{+} + e^{-}, \quad (1)$$

$$\mathrm{Cu}^{+} + \mathrm{Cl}^{-} \rightarrow \mathrm{CuCl}, \quad (2)$$

$$\mathrm{CuCl} + \mathrm{Cl}^{-} \rightarrow \mathrm{CuCl}_2^{-}, \quad (3)$$

$$\mathrm{O}_2 + 2\mathrm{H}_2\mathrm{O} + 4e^{-} \rightarrow 4\mathrm{OH}^{-}. \quad (4)$$

The polarization curve for Al indicates a broad passivation region over which the current density is almost constant followed by a sudden increase. The passive region is attributed to the protective oxide layer on the Al surface, which breaks down at higher potentials, initiating the pitting process. The anodic and cathodic reaction during the localized corrosion of Al is as follows:[37]

$$\mathrm{Al} \rightarrow \mathrm{Al}^{3+} + 3e^{-}, \quad (5)$$

$$2\mathrm{H}^{+} + 2e^{-} \rightarrow \mathrm{H}_2. \quad (6)$$

Two other possible cathodic reactions are hydrogen evolution and oxygen reduction outside of the pits, shown by Eqns. (7) and (8), respectively:

$$2\mathrm{H}_2\mathrm{O} + 2e^{-} \rightarrow \mathrm{H}_2 + 2\mathrm{OH}^{-}, \quad (7)$$

$$\mathrm{O}_2 + 2\mathrm{H}_2\mathrm{O} + 4e^{-} \rightarrow 4\mathrm{OH}^{-}. \quad (8)$$

Tafel extrapolation is used to extract the anodic (b_a) and cathodic (b_c) slopes as well as the corrosion current (I_{corr}). The corrosion rate (ψ) is thus calculated by:

$$\psi = \frac{3.302 I_{\mathrm{corr}} EW}{\rho}, \quad (9)$$

where I_{corr} is the current density in units of [μA/cm^2], EW is the equivalent weight (defined as the atomic weight in [g] divided by the valency), and ρ is the metal density in [g/cm^3]. For Eq. (9), the unit for corrosion rate are [μm/year]. It should be noted that Eq. (9) is only valid for uniform corrosion and not for the localized corrosion. Hence, it is applicable on Cu samples but underestimates the real corrosion rate for Al substrates. To better quantify the corrosion process on our samples, we also measured the corrosion protection efficiency (η), defined as:

$$\eta = \frac{(I_{\mathrm{corr}}^0 - I_{\mathrm{corr}})}{I_{\mathrm{corr}}^0} \times 100\,, \tag{10}$$

where I_{corr}^0 and I_{corr} represent the corrosion current density of the bare and coated substrates, respectively. The measured and calculated data for the samples tested are shown in Table 2. From the polarization curves shown in Figure 5 and the corrosion currents in Table 2, it is worth noting that sol-gel, Parylene C, and superhydrophobic coatings show excellent corrosion resistance. However, the HTMS coating did not show substantial improvement compared to the uncoated samples. This can be attributed to the low thickness of HTMS (~ 3 nm) and existence of pores in the coating that allow the corrosive species (Cl^- ions) to reach to the bare metal surface.[18, 38-39] The sol-gel coating showed very good performance on both Cu and Al substrates. As a test of coating applicability to varying materials, we also applied the sol-gel formulation to 316 Stainless Steel and Cupronickel 70/30, demonstrating good coating quality via visual inspection and surface characterization. Parylene C and AP MO-CVD SiO_2 showed the best corrosion resistance result due to the ultra-high conformality of the coating stemming from the CVD application method (see Methods). The use of CVD allows for a very low density of pinholes at the surface and creates a large charge transfer resistance at the electrolyte-coating interface. The AP MO-CVD SiO_2 had the lowest corrosion current on Cu while Parylene C was showing a better performance on Al

substrates. Cu has higher reactivity with NaCl solution compared to Al, leading to higher sensitivity of Cu to the existence of pinholes. Therefore, we hypothesized that the elevated temperature (300°C) AP MO-CVD SiO_2 coating formed less pinholes compared to the room temperature Parylene C deposition. Conversely, on Al substrates, the thicker Parylene C coating protected the surface better compared to the 400 nm AP MO-CVD SiO_2 coating, even with potentially lower pinhole density. Finally, the addition of the SOCAL functional coating on the free sol-gel interface did not result in any added corrosion resistance compared to the sol-gel only coating.

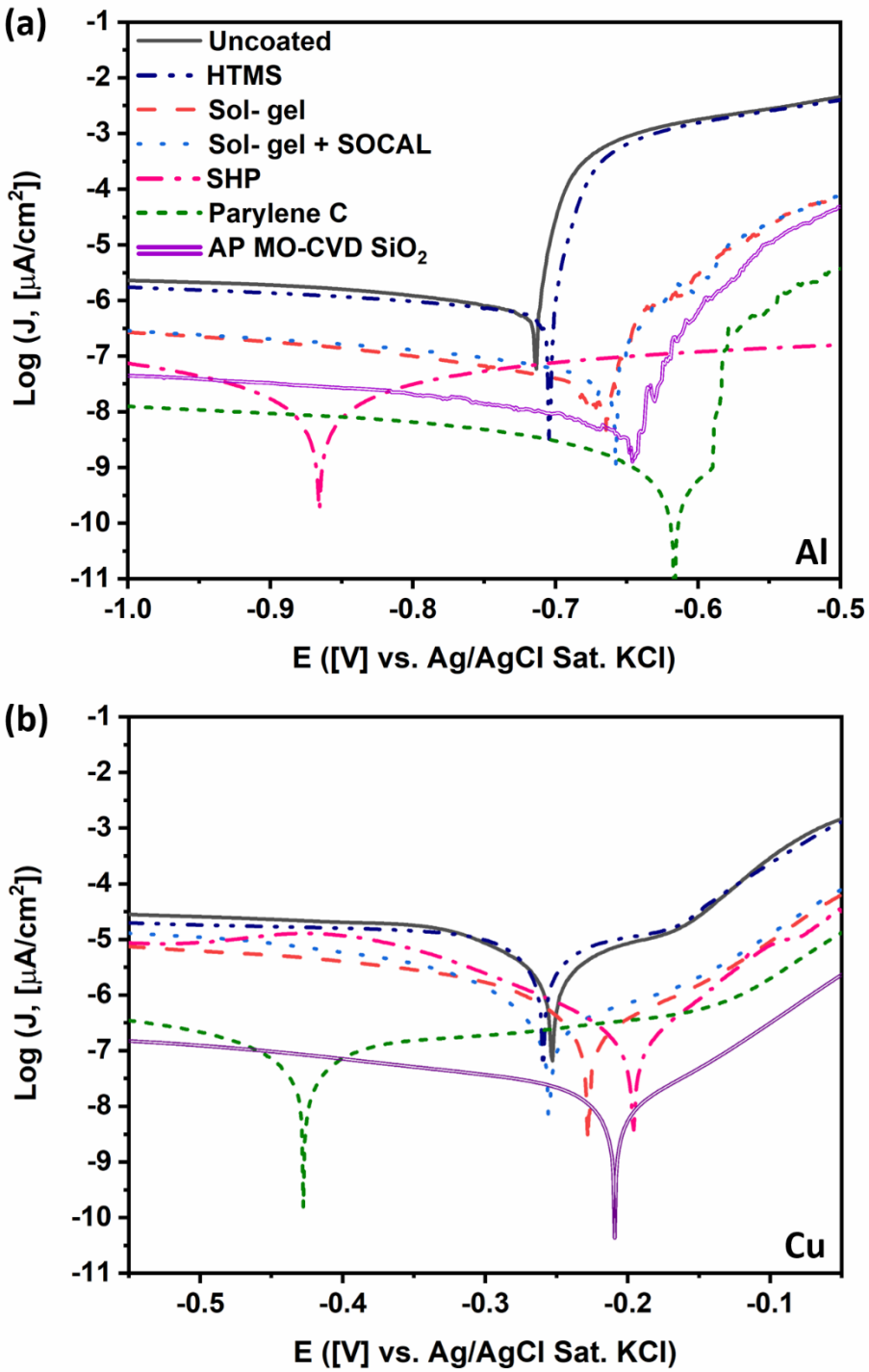

Figure 5. Tafel polarization curves for polished (a) Cu and (b) Al substrates having differing corrosion protection coatings (listed in the legend of b). Error bars are not shown in the experimental data as the measurement uncertainty is smaller than the thickness of the individual lines. The uncertainty in potential is ±1mV ± 0.2% of the reading, and the current is 0.75% of the reading. The legend in (a) is valid for both graphs.

Table 2. Tafel fit parameters of Cu and Al substrates for a variety of coatings tested in 3 wt.% NaCl and 0.5 M NaCl, respectively.

Substrate	Coating	E_{corr} [V]	I_{corr} [μA/cm^2]	b_a [mV/dec]	b_c [mV/dec]	ψ [μm/yr]	η [%]	Error [%]
Cu	Uncoated	-0.253	4.20	170.1	136	48.67	0	0
	HTMS	-0.272	3.58	140.4	193.1	41.58	14.56	2
	Sol-gel	-0.228	0.17	82.1	55.1	1.97	95.95	13
	Sol-gel+SOCAL	-0.255	0.20	114.2	50	2.38	95.11	13
	SHP	-0.196	0.10	49.6	82	1.17	97.62	14
	Parylene C	-0.427	0.06	120.1	114.2	0.65	98.67	14
	AP MO-CVD SiO_2	-0.209	0.019	142.4	164.3	0.22	99.54	14
Al	Uncoated	-0.714	0.64	44	303.3	6.99	0	0
	HTMS	-0.704	0.58	30.8	436.8	6.40	8.49	1
	Sol-gel	-0.664	0.029	20.7	233.5	0.32	95.48	13
	Sol-gel+SOCAL	-0.658	0.035	37	186.2	0.38	94.52	13
	SHP	-0.866	0.012	197	144.6	0.13	98.14	14
	Parylene C	-0.616	0.002	2.27	355.4	0.022	99.68	14
	AP MO-CVD SiO_2	-0.646	0.005	22.4	267.5	0.056	99.2	14

Electrochemical Impedance Spectroscopy (EIS): As a complementary electrochemical technique used to help understand the charge transfer mechanisms through the various coatings, EIS was used to further investigate the performance of the different coatings on Al and Cu substrates. Nyquist plots demonstrating the results are shown in Figure 6a, b, showing the imaginary impedance (Im(Z)) as a function of the real impedance (Re(Z)). In general, the Nyquist plot can be analyzed by locating the impedance intercept with the real axis at high frequency to determine the solution resistance (R_s), and the intercept with the real axis at low frequency to determine the charge transfer resistance (R_{ct}),[40] and coating resistance R_c to ion transfer. The latter

is dependent to the density of pinholes and defects on the protective coating. Thus, a bigger diameter for the curve illustrates better corrosion resistance.

As a secondary quantification of corrosion resistance, we plot the Bode plots in Figure 6c-f. In a typical Bode plot, the impedance (|Z|) is plotted as a function of the ac input frequency, with higher impedance at low frequencies indicating better corrosion resistance. A phase diagram can also elucidate the coating corrosion resistance. At high frequency, if the resistance of the coating is high, the signal shows a capacitive behavior with a phase angle of -90°. Conversely, if the corrosion resistance is low, the coating is equivalent to a resistor with a phase angle is 0°.[41]

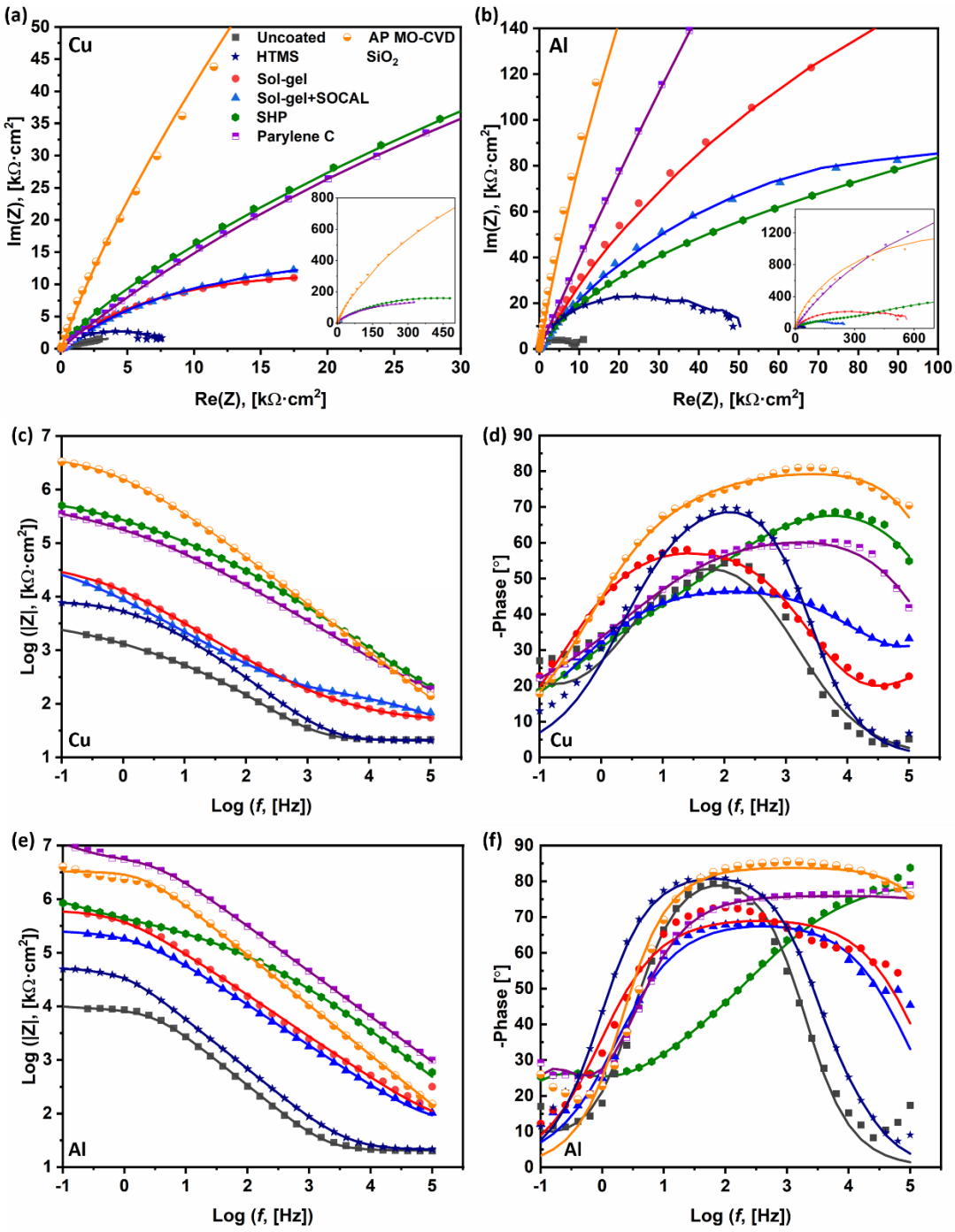

Figure 6. EIS Nyquist plots for (a) polished Cu substrates in 3 wt.% NaCl solution and (b) polished Al substrates in 0.5 M NaCl solution. Insets: Nyquist plots data for a larger range of impedance. The inset axis labels are the same as in the main plots and have been removed for clarity. (c-f) EIS Bode plots obtained in 3 wt.% NaCl solution and 0.5 M NaCl solution for Cu and Al substrates, respectively. Bode (c) impedance and (d) phase plots for Cu substrates. Bode (e) impedance and (f) phase plots for Al substrates. The legend presented in (a) is valid for all graphs. The solid lines represent fits based on the models (Fig. 5). The uncertainty bars for each data point are smaller than the symbols used and are not shown for clarity.

To quantify the corrosion mechanisms for each coating, we developed equivalent electrical circuits to model the uncoated, coated, and superhydrophobic samples capable of fitting the experimental EIS data. The equivalent circuits are shown in Figure 7. Due to the non-ideal capacitive behavior of the coating, capacitance elements are replaced with constant phase elements (CPE) and the impedance (Z_{CPE}) defined by the following equation:

$$Z_{\mathrm{CPE}} = \frac{1}{Q(j\omega)^n}, \tag{11}$$

where Q is the CPE constant, ω is the angular frequency, and n is the CPE exponent. The CPE represents an ideal capacitor when $n = 1$ and an ideal resistor when $n = 0$. A decrease from $n = 1$ represents non-uniform current distribution which arises from surface inhomogeneity and defects.[42]

For uncoated metals (Fig. 7a), $\mathrm{CPE_{dl}}$ refers to the capacitive double layer formed at the metal/solution interface and $\mathrm{R_{ct}}$ is the charge transfer resistance. Here, w is the Warburg element which models semi-infinite linear diffusion and represent itself as a straight line with the slope of 45° in the Nyquist plot (Fig. 6a, b). For the coated metals (Fig. 7b), $\mathrm{CPE_c}$ is the capacitance caused by the formation of the double layer at the coating/solution interface, and R_{c} is the coating resistance which is dependent to the density and size of pinholes and defects in the coating which allow ions to pass through it and reach to the metallic substrate. Therefore, R_{c} approaches infinity for a perfect pinhole-free coating.

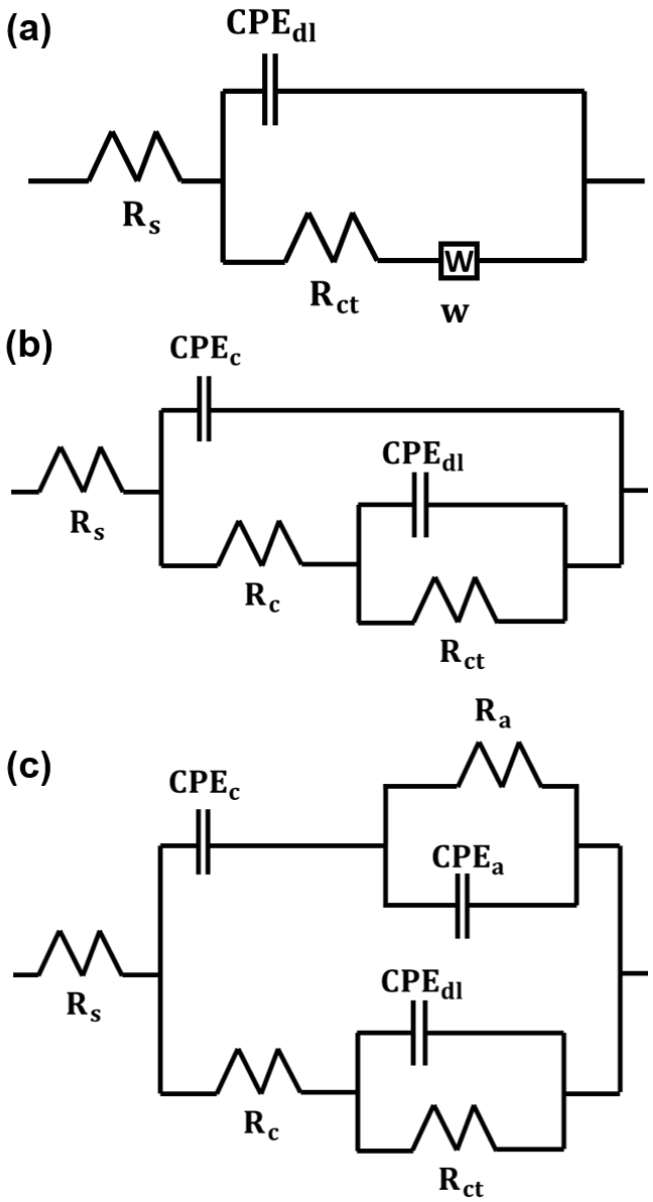

Figure 7. Equivalent circuit diagrams used to model the EIS experiments. Circuit diagram for the (a) uncoated, (b) coated smooth, and (c) superhydrophobic rough samples. The parameter CPE_c is a constant phase element at the coating/solution interface with units of [$\mu F \cdot s^{a-1} \cdot cm^{-2}$], CPE_{dl} is the constant phase element at the metal/solution interface with units of [$\mu F \cdot s^{a-1} \cdot cm^{-2}$], CPE_a is the constant phase element of the air pockets for the rough superhydrophobic coatings with units of [$\mu F \cdot s^{a-1} \cdot cm^{-2}$], R_{ct} is the charge transfer resistance in units of [$\Omega \cdot cm^2$], R_c is the coating corrosion resistance [$\Omega \cdot cm^2$], R_a is the resistance caused by air pockets for rough superhydrophobic coatings in units of [$\Omega \cdot cm^2$], R_s is the solution electrical resistance in units of [$\Omega \cdot cm^2$] and *w* is the Warburg element in units of [$\Omega \cdot cm^2 \cdot s^{-1/2}$]. CPE is defined in Eq. (11). The "a" value in the CPE unit is different for every coating and is summarized for each coating in Table 4.

When the ions diffuse into the coating, we assume that on the metal side of the path, an area of the coating is delaminated and a region with electrolyte has formed. The $\mathrm{CPE_{dl}}$ and R_{ct} terms are associated to the formation of these regions and they differ greatly from what is formed at the uncoated substrate. In Figure 7c, R_{a} and $\mathrm{CPE_a}$ are labeled on the circuit to include the resistance and constant phase element caused by the air pockets trapped in the micro/nanostructures. Here, R_{a} consists of three components: air resistance, coating resistance (R_{c}) and charge transfer resistance at the surface (R_{ct}). In order to exclude the effects of the coating resistance stemming from only the boehmite layer on the Al substrates and CuO layer on the Cu substrates, we conducted the same EIS experiments on superhydrophilic surfaces with no functional coatings. Although the protective boehmite and CuO layers increase the corrosion resistance compared to the bare polished substrates, the superhydrophobic samples show much larger corrosion resistance compared to superhydrophilic samples due to the presence of trapped air within the superhydrophobic structures. The polarization curves as well as Bode and Nyquist plots of superhydrophilic surfaces are provided in Figure 8.

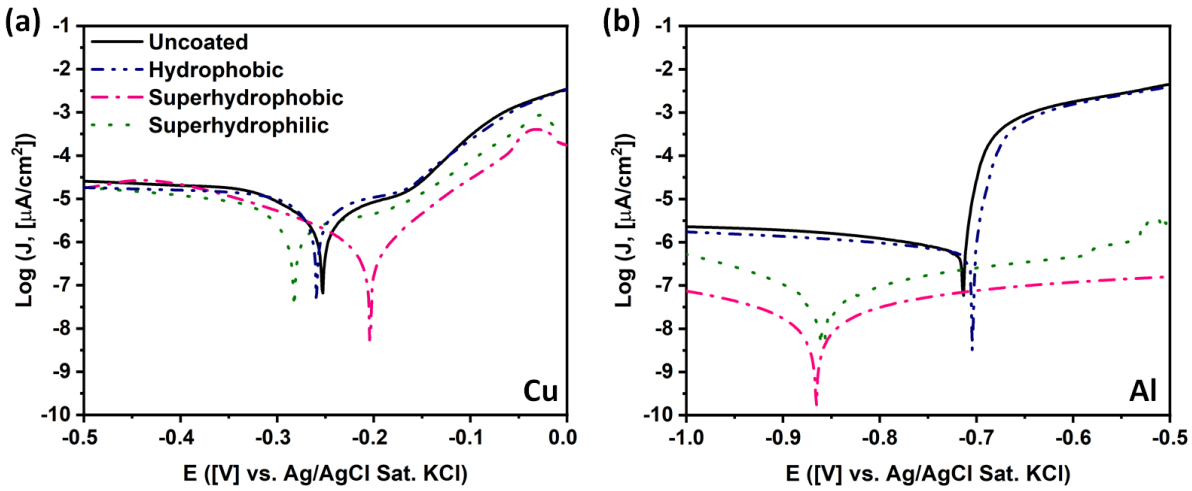

Figure 8. Polarization curves of hydrophilic (Uncoated), hydrophobic (HTMS), superhydrophobic and superhydrophilic (a) Cu and (b) Al. The legend in (a) is valid for (b). The results of the superhydrophilic surface is shown along with other surfaces for comparison. The measurements were done at room temperature in a 3 wt.% NaCl and 0.5 M NaCl solution for Cu and Al substrates, respectively.

The parameters extracted from the fitted circuits for different coatings on Al and Cu substrates are shown in Table 3. In Table 3, the corrosion protection efficiency (H) for coated samples is defined as:

$$\mathrm{H} = \frac{(R_{\mathrm{ct}} + R_{\mathrm{c}}) - R_{\mathrm{ct}}^{0}}{(R_{\mathrm{ct}} + R_{\mathrm{c}})} \times 100\,, \tag{12}$$

where R_{ct}^{0} is the charge transfer resistance of the uncoated substrate. To model the superhydrophobic surface, Eq. (12) is modified to account for the effect of air pocket resistance:

$$\mathrm{H} = \frac{R_{\mathrm{eq}} - R_{\mathrm{ct}}^{0}}{R_{\mathrm{eq}}} \times 100\,, \tag{13}$$

where R_{eq} is the equivalent resistance at the superhydrophobic surface and is calculated by:

$$R_{\mathrm{eq}} = \frac{1}{\frac{1}{R_{\mathrm{ct}} + R_{\mathrm{c}}} + \frac{1}{R_{\mathrm{a}}}}\,. \tag{14}$$

Equation (14) is derived by analysis of the superhydrophobic interface with the electrolyte, which shows that two possible paths for the corrosive species to attack the surface exist, and that the corresponding ionic resistances of these paths is parallel.

Table 3. EIS parameters of Cu and Al substrates with different coatings. The electrolyte for Cu and Al substrates is 3 wt.% NaCl and 0.5 M NaCl, respectively. The symbols a, b and c are the exponents of $\mathrm{CPE_{dl}}$, $\mathrm{CPE_c}$ and $\mathrm{CPE_a}$, respectively. Units of R, $\mathrm{CPE_c}$, and $\mathrm{CPE_a}$, and w are [$\Omega\cdot\mathrm{cm}^2$] and [$\mu\mathrm{F}\cdot\mathrm{s}^{a-1}\cdot\mathrm{cm}^{-2}$], and [$\mu\mathrm{F}\cdot\mathrm{s}^{b-1}\cdot\mathrm{cm}^{-2}$], [$\Omega\cdot\mathrm{cm}^2\cdot\mathrm{s}^{-1/2}$], respectively.

Substrate	Coating	R_{s}	R_{ct}	$\mathrm{CPE_{dl}}$	a	$\mathrm{CPE_c}$	b	R_{c}	R_{a}	$\mathrm{CPE_a}$	c	W	H [%]
Cu	Uncoated	18.96	1712	89.57	0.69	-	-	-	-	-	-	713.3	0
	HTMS	16.41	7556	6.01	0.92	22.1	0.61	5.0	-	-	-	-	77.36
	Sol-gel	16	38220	16.34	0.68	2.08	0.66	59.46	-	-	-	-	95.53
	Sol-gel+SOCAL	13.67	47920	20.68	0.68	11.3	0.54	183.4	-	-	-	-	96.44
	SHP	60.03	852000	1.152	0.44	0.17	0.79	0.0071	1.06E6	0.049	1	-	99.64
	Parylene C	69.04	1212000	2.02	0.26	0.55	0.71	795.2	-	-	-	-	99.86

Table 3. (Cont.)

Al	AP MO-CVD SiO_2	30.15	4439000	0.119	0.48	0.054	0.89	194600	-	-	-	-	99.96
	Uncoated	16.89	9997	6.4	0.91	-	-	-	-	-	-	5637	0
	HTMS	21.1	52369	2.89	0.86	1.16	0.99	28.45	-	-	-	-	80.92
	Sol-gel	14.9	597600	0.32	0.79	0.026	0.95	404.9	-	-	-	-	98.32
	Sol-gel+SOCAL	16.02	250900	0.62	0.77	0.013	0.99	133.5	-	-	-	-	96.02
	SHP	14	1821000	0.57	0.41	0.010	0.92	26.35	1.306E6	0.382	0.81	-	98.77
	Parylene C	14.01	9674000	0.18	0.91	0.014	0.85	6545000	-	-	-	-	99.94
	AP MO-CVD SiO_2	20.62	1104000	0.0053	0.97	0.027	0.93	3306000	-	-	-	-	99.77

The Bode and Nyquist plots as well as the fitted data shown in Table 3 show that all coatings studied, with exception of HTMS, show significant improvement in corrosion protection. The results indicate that the effect of SOCAL added to the sol-gel SiO_2 is negligible in terms of added corrosion protection. The model results are in excellent agreement with the experimental results obtained from the potentiodynamic polarization characterization. Parylene C shows the best performance with a very large R_c compared to the sol-gel coating. The difference is mainly dictated by the differences in the coating processes. Parylene C is coated on the Al and Cu substrate using CVD at elevated temperatures which gives a very conformal coating leading to smaller defect and pinhole densities. Conversely, sol-gel is coated via facile dip coating at room temperature which is more prone to pore or defect formation in the coating.

To achieve a better comparison between the corrosion protection of Parylene C and SiO_2 on Cu and Al, in addition to benchmarking the corrosion resistance with a commercially available coatings, we applied 400 nm of SiO_2 through AP MO-CVD. The coating was obtained from Wieland Wicoatec GmbH, Germany. The model suggests that the main mode of corrosion protection offered by the Parylene C and AP MO-CVD SiO_2 coatings is through the high charge transfer resistance stemming from their highly electrical insulating properties. The R_{ct} for Parylene

C on Al and AP MO-CVD SiO_2 on Cu are the highest among the coatings tested, showing a very low density of pinholes inside the coating which makes the path for electron transfer between the corrosive ions and metallic substrate difficult. As shown in SEM images of the sol-gel coating (Fig. 3), existence of pinholes allows corrosive species to penetrate into the coating and react with the substrate to cause coating delamination at the substrate/coating interface. The superhydrophobic coating mainly protects the surface by decreasing the available surface area for corrosion reaction, also manifesting itself in the R_{ct} which is a function of available area. The high R_{a} indicates the well-maintained Cassie- Baxter state of superhydrophobicity which is successful in repelling the solution from the surface. The hydrophobic and superhydrophobic coating failure occurred initially with the degradation of the functional coating. Even not in a corrosive environment, silane monolayers are known to be chemically unstable in aqueous envrionment and can be desorbed from the substrate within hours[43], mainly due to the hydrolysis reaction between the Si-O-X bond and water that breaks the bond chemcially.[44] When exposed to corrosive media sea water, the ultra-thin (~ 3 nm) silane functional coating degrades rapidly due to the weak bonding to the metallic substrates. When the hydrophobic silanized surface is immersed in sea water solution, it was observed that hydrophobicity was lost before the corrosion initiated visually on the metal. The same failure mode was observed on the SOCAL, where the slippery property of the surface was lost after immersing the Cu-coated coupon in sea water solution for 12 hours, with the $\Delta\theta$ increaseing dramatically, indicating the SOCAL removal from the substrate. The Superhydrophobic coating, however, had an advantage over the hydrophobic coating due to the following reasons. Firstly, the functional coating more readily bonds to the CuO layer.[45] Second, the trapped air in the nanostructures acts as a barrier to corrosion. The corrosion mechanism observed on the sol-gel coating can be attributed to pinholes and microcracks in the coating. The

corrosion will initially take place at pinholes, generating osmotic pressure leading to coating delamination.[46] Other mechanisms of the coating degradation do not necessarily need corrosion to initiate. In this mechanism, a water blister is formed at the pinhole location, accumulating the solution beneath the coating, causing delamination.[18] Nevertheless, decreasing the size and density of pinholes is the main challenge for enhancing polymeric coating corrosion resistance.

CHAPTER 5: FLOW CORROSION

To demonstrate the scalability of the coatings as well as the durability to harsher conditions than those encountered during EIS, we tested internally coated Cu tubes in a custom-built corrosion flow loop with sea water (40% salinity) as the corrosive fluid inside the loop. The corrosion flow loop tests were conducted with the fluid at room temperature (21°C) and at 40°C. Note that the SOCAL coating did not alter the anti-corrosion performance of the sol-gel coating, with the measurable corrosion resistance difference being negligible. Therefore, only one of the samples is shown in Figure 9 for clarity.

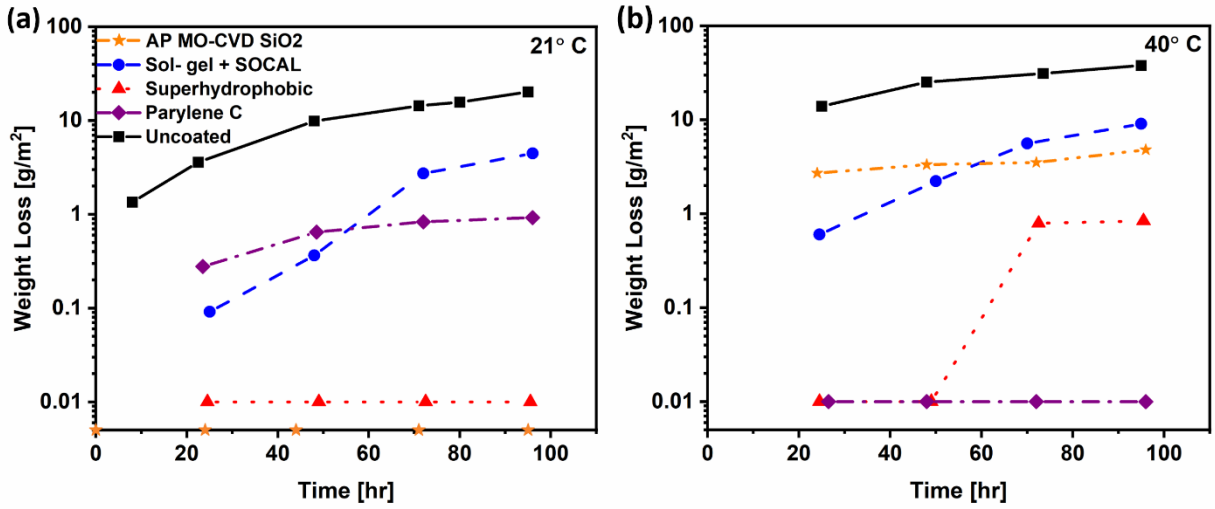

Figure 9. Corrosion flow loop test results with sea water (40% salinity) used on internally coated Cu tubes with internal single-phase laminar flow ($Re_D \approx 600$) and (a) 21°C and (b) 40°C inlet fluid temperatures. The legend in (a) applies for (b). Measurement uncertainty was ±0.64 g/m^2 and is not shown for clarity.

The flow corrosion tests revealed that at room temperature and 40°C, a negligible amount of weight loss occurred for the sol-gel coated tubes in the first 48 and 24 hours, respectively. At the end of the 4 days flow period, the sol-gel coated Cu tube showed 78% less weight loss at room temperature and 76% less at 40°C when compared to the uncoated Cu tubes. The reduction in weight loss when compared to the uncoated Cu tube was >95% for the Parylene C and

superhydrophobic CuO tubes. After each test, the tube was cut longitudinally to investigate the internal area of the tube and to observe the change in wall roughness morphology. As expected, the uncoated Cu tube completely oxidized. Conversely, the coated tubes looked similar to their pristine condition prior to testing. Table 4 shows the instrumentation details of the flow corrosion loop. The flow corrosion experimental setup is shown in Figure 10.

Table 4. Details of the instrumentation on the corrosion flow loop setup.

Measurement	Instrument	Span	Uncertainty
Temperature	T-Type Thermocouple	0 to 315ºC	± 0.5ºC
Pressure Drop	Differential Pressure Sensor, Rosemount 3051CD	± 6.2 kPa	± 0.1% of Span
Mass Flow Rate	Coriolis Mass Flow Meter, Micromotion Elite Series, CMFS015M	0 to 330 kg/hr	± 0.1% of Reading
Mass	Microbalance, Radwag AS 220	0 to 220 g	± 0.1 mg
Tube Length	Ruler	0 to 30 cm	± 1 mm
Tube Diameter	Measurement Provided by Vendor	-	± 0.1 mm

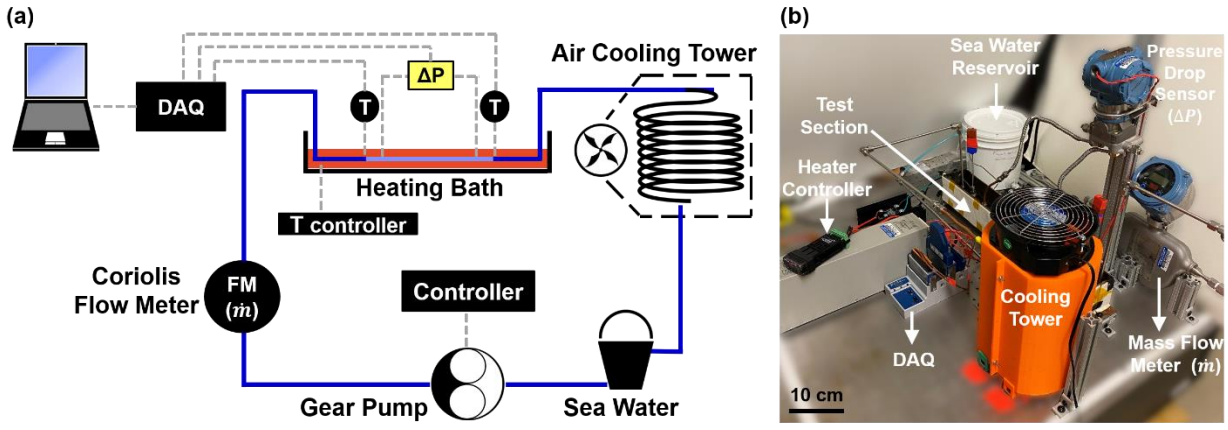

Figure 10. (a) Schematic and (b) photograph of the corrosion flow loop setup. The labels denoted by DAQ, ΔP and T in the schematic correspond to the data acquisition system, differential pressure transducer, and thermocouple sensors, respectively.

CHAPTER 6: CYCLIC CORROSION TESTING

Cyclic corrosion testing is one of the common ways to measure the corrosion resistance of heat exchanger materials, both for tube and fin alloys.[47] Therefore, we tested Cu substrates coated with HTMS, superhydrophobic Cu substrates, as well as sol-gel SiO_2 and Parylene C coated Cu substrates for 4 consecutive days (identical to the flow corrosion experiment duration). To emulate aggressive corrosion conditions, we utilized the ASTM G85 sea water acetic acid test (SWAAT) test which is commonly used in multiple industries to evaluate salt corrosion performance of components.[48] The results of the cyclic corrosion test are shown in Table 5. Based on the results, the largest weight loss that was observed was for the sol-gel coated Cu substrates. The high mass loss was due to the blister and crack formation in the sol-gel coating. The blisters and cracks cause the coating to completely peel from the surface after ultra-sonication in acetone. Another reason for the higher weight loss of the coated samples (other than Parylene C) when compared to the uncoated sample was due to the higher adhesion of corrosion products and salts to the uncoated sample, some of which may remain on the surface even after the utilized cleaning procedure after testing. The observed trends can be identified by observing images of the surfaces before and after the cleaning procedure (Fig. 11).

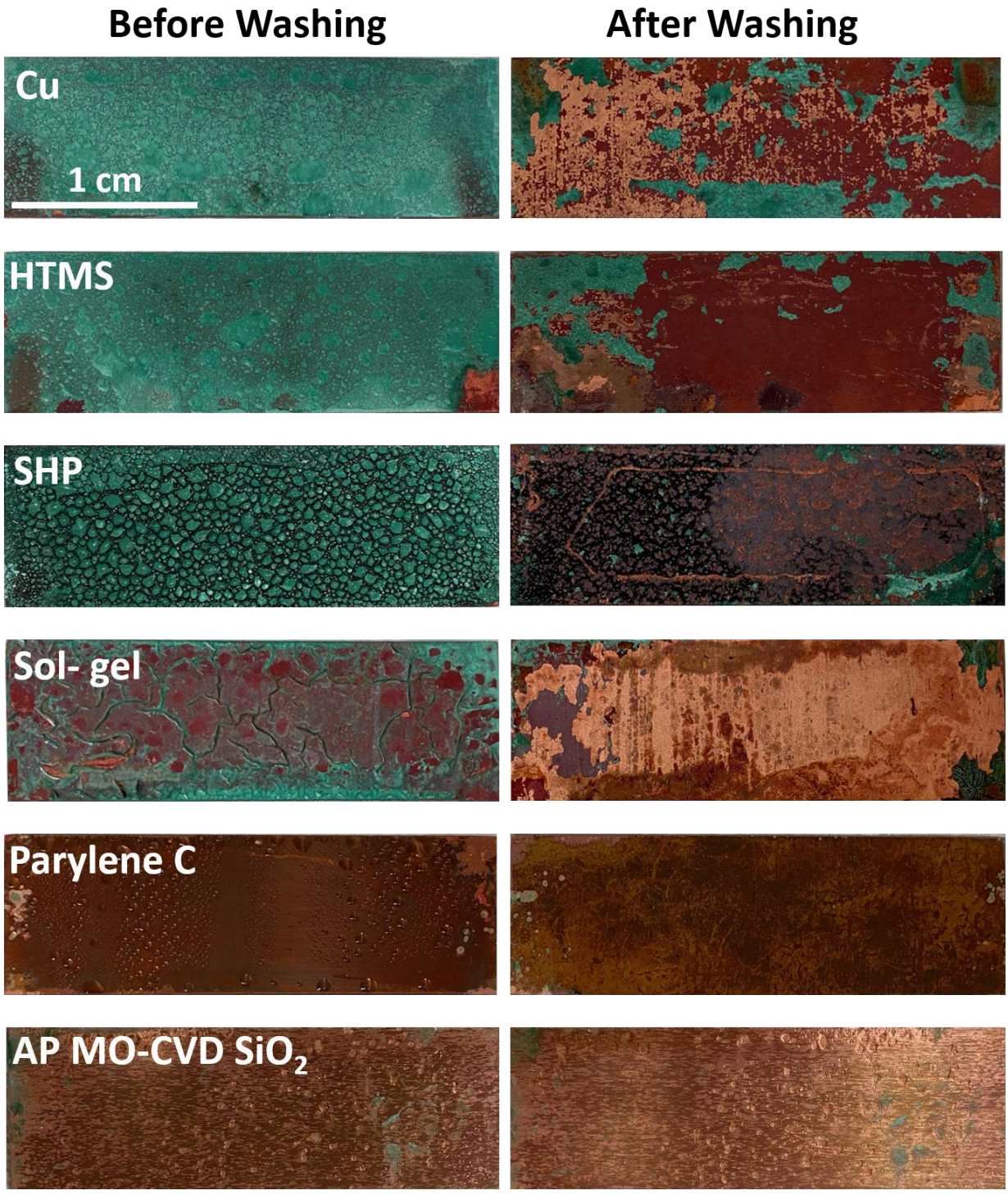

Figure 11 Optical close-up images of uncoated, HTMS coated, superhydrophobic coated, sol-gel coated, Parylene C, and AP MO-CVD SiO_2 coated Cu substrates after the SWAAT for four days. Left column images are immediately after bringing the samples out of the corrosion chamber. Right column images are after drying and cleaning the samples.

Parylene C showed the lowest corrosion rate and no coating delamination was observed after the 4-day test. AP MO-CVD SiO_2 coating is showing a good performance similar to Parylene C. This similar performance can be attributed to the CVD method used for coating deposition which leads to a pinhole free surface. The better performance of Parylene C is because of the almost 7 times thicker coating. The Parylene C coated sample was kept for 30 days under the test condition and it lost approximately 1 g/m^2 of its initial weight, indicating that the coating is still functional. However, some damages were observed at the edges of the tab and small portion of the coating was peeled off at the edges.

Table 5. Cyclic corrosion test results of the uncoated, HTMS-coated, superhydrophobic (SHP), sol-gel-coated, and Parylene C coated polished Cu substrates after 4 days of SWAAT testing.

Sample	Initial Mass [g]	Final Mass [g]	Mass Loss [g/m^2]
Uncoated	26.326	26.253	33.877
HTMS	26.180	26.064	54.513
SHP	26.498	26.393	41.879
Sol-gel	26.362	26.199	76.178
Parylene C	26.214	26.213	0.421
AP MO-CVD SiO_2	13.8329	13.831	0.889

A photograph of the cyclic corrosion tester is shown in Figure 12.

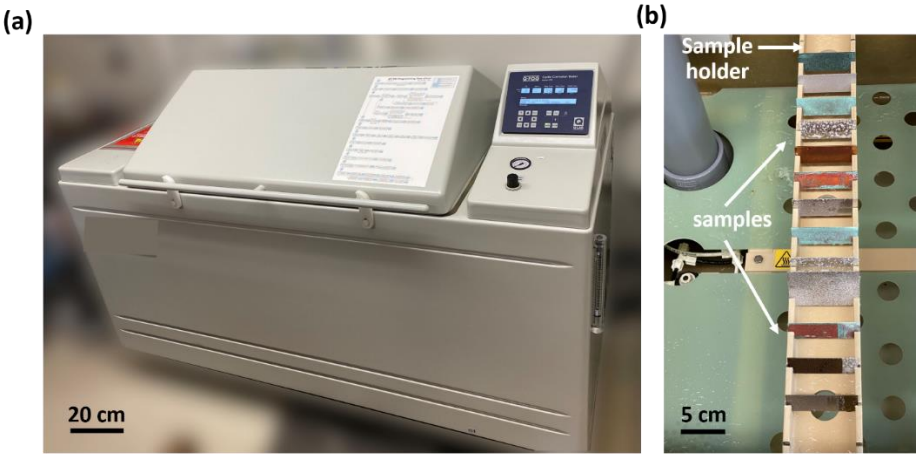

Figure 12. Photograph of the (a) outside and (b) inside of the Q-FOG cyclic corrosion tester. The image showing the inside (b) demonstrates the placement of the samples on the sample holder.

CHAPTER 7: HEAT TRANSFER ANALYSIS

Flow corrosion testing is a complementary method to the electrochemical characterization as it captures the corrosion protection efficacy of the coatings for long time usage in harsher working conditions consisting of viscous shear forces caused by the movement of sea water. One of the most promising applications for corrosion-prevention coatings is in heat transfer equipment. Thermal systems such as boilers, evaporators, condensers, can suffer from corrosion due to the moisture present in the flowing working fluids. However, the addition of a corrosion-protective coating has drawbacks. The coating will act as an additional barrier to heat transfer and will increase the overall thermal resistance. To study the effects of coating application on overall heat transfer, we begin by assuming that our sol-gel coating has identical thermal conductivity to what has been reported for amorphous SiO_2,[49-50] or $k_{SiO_2} \approx 1.3$ W/(m·K). As a comparison, we also analyzed the added thermal resistance of adding the Parylene C coating as a corrosion prevention strategy, with the thermal conductivity of Parylene C being $k_{\text{parylene}} \approx 0.08$ W/(m·K).[51-52] Considering the Cu tube dimensions for the tests conducted here (ID = $D = 2r_i = 3$ mm, OD = $2r_o = 5$ mm) with convection occurring on both inner and outer surfaces of the tube, the total heat transfer resistance across the uncoated tube can be calculated as:

$$R_{\text{total}} = R_{\text{out}} + R_{\text{conduction}} + R_{\text{in}} = \frac{1}{2\pi r_o L h_{\text{out}}} + \frac{\ln\left(\frac{r_o}{r_i}\right)}{2\pi k L} + \frac{1}{2\pi r_i L h_{\text{in}}}, \quad (15)$$

where h_{out} and h_{in} are the convective heat transfer coefficients on the outside and inside surfaces of the tube, L is the tube length, and k is the thermal conductivity of the tube material. For the coated tubes, the resistance of the coating needs to be added to the total thermal resistance. Assuming that both internal and external sides of the tube are coated with the same thickness (t) of the coating having an isotropic thermal conductivity of k_{coating}, the total resistance becomes:

$$R_{\text{total}} = \frac{1}{2\pi r_{\text{o}} L h_{\text{out}}} + \frac{\ln\left(\frac{r_{\text{o}}+t}{r_{\text{o}}}\right)}{2\pi k_{\text{coating}} L} + \frac{\ln\left(\frac{r_{\text{o}}}{r_{\text{i}}}\right)}{2\pi k L} + \frac{\ln\left(\frac{r_{\text{i}}}{r_{\text{i}}-t}\right)}{2\pi k_{\text{coating}} L} + \frac{1}{2\pi r_{\text{i}} L h_{\text{in}}}\ , \tag{16}$$

The overall heat transfer coefficient (U) is the inverse of the total thermal resistance. Taking the ratio of overall heat transfer coefficient of a coated tube to an uncoated tube, it is possible to quantify the effect of the coating thickness and its thermal conductivity.[21] The conductance ratio is shown in Equation (17) as:

$$\frac{U_{\text{uncoated}} - U_{\text{coated}}}{U_{\text{uncoated}}} = \frac{\ln\left(\frac{r_{\text{i}}(r_{\text{o}}+t)}{r_{\text{o}}(r_{\text{i}}-t)}\right)}{2\pi a L k_{\text{coating}} + \ln\left(\frac{r_{\text{i}}(r_{\text{o}}+t)}{r_{\text{o}}(r_{\text{i}}-t)}\right)}\ , \tag{17}$$

where,

$$a = \frac{k(r_{\text{i}} h_{\text{in}} + r_{\text{o}} h_{\text{out}}) + r_{\text{i}} r_{\text{o}} h_{\text{in}} h_{\text{out}} \ln\left(\frac{r_{\text{o}}}{r_{\text{i}}}\right)}{2\pi L (r_{\text{i}} r_{\text{o}} h_{\text{in}} h_{\text{out}} k)}. \tag{18}$$

The decrease in the overall heat transfer coefficient as a function of SiO_2 and Parylene C thicknesses is shown in Figure 13. Three different outside conditions were considered for the analysis. The first condition was forced convection on finned tubes having a 10X higher external heat transfer area, characteristic of liquid-to-air heat exchangers. The effect of fins was included in Equation (17) and (18) by implementing a 10X increase on the outside heat transfer area. The second case was for a tube-in-tube heat exchanger undergoing single-phase liquid flow in which the outside and inside convective heat transfer coefficients are identical ($h_{\text{out}} = h_{\text{in}}$). The third case was for condensation heat transfer on the outside the tube with $h_{\text{out}} = 20$ kW/(m^2·K). For laminar flow inside the tube, we assumed a fully developed Nusselt number of 3.66 (Nu_D = 3.66) and for turbulent flow, the Petukhov[53] correlation was used to calculate the convective heat transfer coefficient.

Assuming a 3 μm thick SiO_2 sol-gel coating, identical to what was used in the corrosion flow loop tests, on Cu tubes (ID = 3 mm, OD = 5 mm) with thermal conductivity k = 385 W/(m·K), natural convection heat transfer coefficient to air on the outside of the ($h_{out} \approx 25$ W/(m^2·K)) and laminar single-phase liquid flow on the inside of the tubes ($Nu_D = h_{in}D/k = 3.66$, $h_{in} \approx 700$ W/(m^2·K)), the decrease in overall heat transfer coefficient is approximately 0.015% compared to the uncoated tube. However, the decrease when using Parylene C with the same thickness was 0.24%, 16 times greater when compared to the SiO_2 due to the higher intrinsic thermal conductivity of glass when compared to the majority of polymers.

Our analysis shows that although Parylene C shows the best corrosion resistance, it also has the highest potential to degrade heat transfer due to its low thermal conductivity, a significant consideration for many thermal systems having high conductance. For applications which have limitations in heat transfer (such as air-side applications), the Parylene C coating represents a promising coating methodology that is both durable and highly efficient at preventing corrosion.

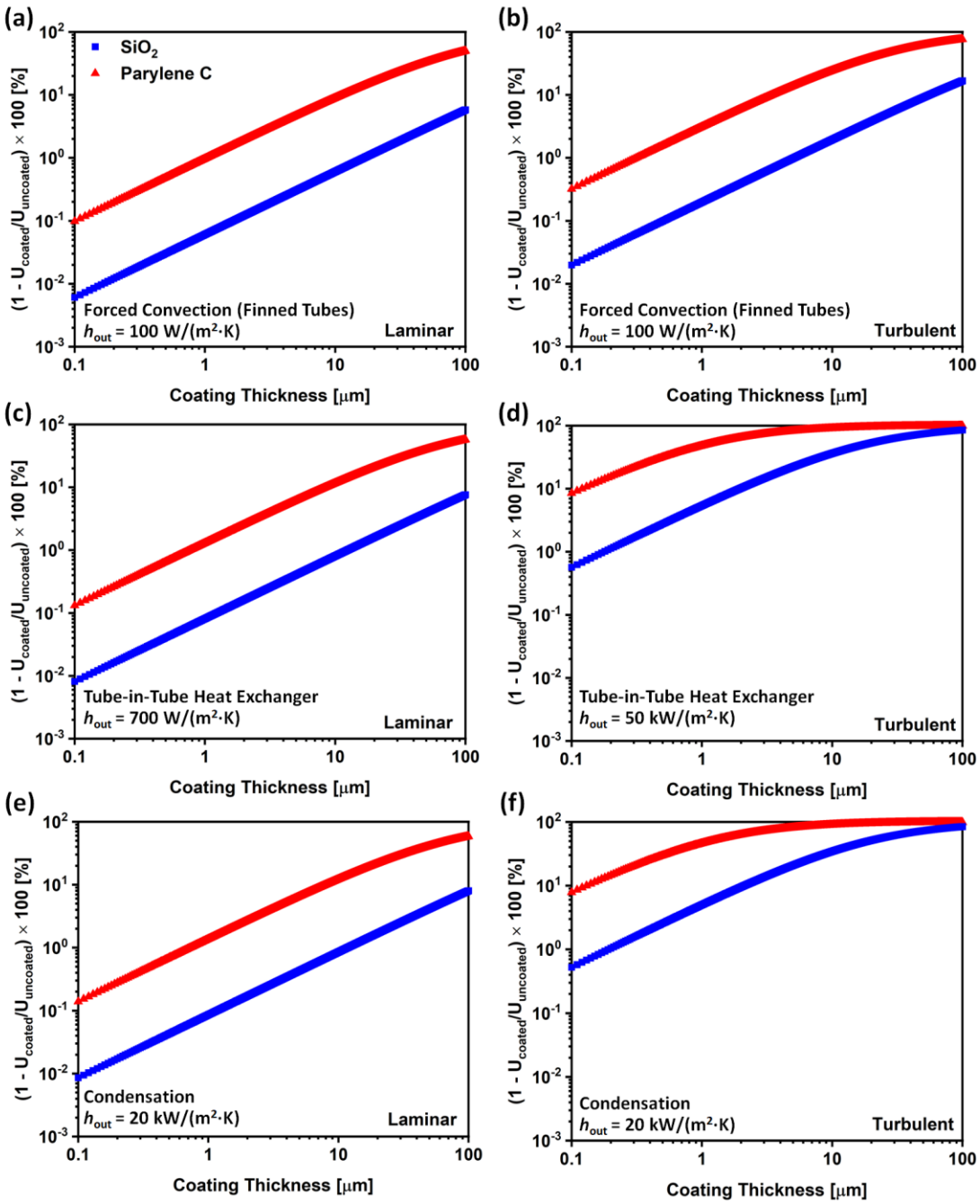

Figure 13. Decrease of the overall heat transfer coefficient due to the added thermal resistance of the addition of the corrosion prevention coating. The results are based on Cu tubes used in the corrosion flow loop setup (r_o = 2.5 mm, r_i = 1.5 mm, k = 385 W/(m·K) and two different working conditions assumed: (a, c and e) laminar flow inside the tubes, h_{in} = 700 W/(m^2·K) with Nu_D = 3.66, and (b, d and f) highly turbulent flow (h_{in} = 50 kW/(m^2·K). See section S10 of Supporting Information for the Petukhov correlation used in turbulent flow. For (a) and (b), the external boundary condition is air forced convection on finned tubes (h_{out} = 100 W/(m^2·K)). For (c) and (d), we modeled the tube-in-tube heat exchanger case in which h_{out} = h_{in}. For (e) and (f), we modeled condensation on the outside of the tubes (h_{out} = 20 kW/(m^2·K)).

CHAPTER 8: DISCUSSION

An important consideration when selecting a corrosion prevention mitigation is the cost of the coating material as well as the cost of the process required to implement the coating process. For a conformal Parylene C, a high temperature vacuum-compatible CVD chamber is required. This leads to large capital expenditure as well as a time-consuming process, consisting of pumping down the chamber, increasing the temperature and allowing Parylene C to vaporize and deposit on the substrate. For the Parylene C depositions tested here, the deposition rate is approximately 17 nm/minute, which requires approximately 5 hours to deposit a coating of 5 μm thickness, which will be durable enough to withstand operational conditions for more than a few months. For every deposition process, a constant 1- hour time is required for warming up and cooling down the system. Temperatures as high as 690°C were required to cleave the dimeric Parylene gas to its monomeric form, however the deposition was done at ambient temperature. Conversely, deposition of AP MO-CVD SiO_2 was done at 300°C.

In addition to monetary and time cost, scalability is another challenge when vacuum chambers are required for coating application. The necessity for vacuum systems adds costs (both equipment cost and time) to the entire manufacturing process. On the other hand, the equipment cost as well as the process time for superhydrophobic surface fabrication and sol-gel coating are much lower. The superhydrophobic Al and Cu surfaces presented in this work are fabricated through two facile steps: making micro/nanostructures using chemical etching followed by applying functional coating through an atmospheric pressure CVD process. The latter is done in an atmospheric pressure chamber at 80°C, requiring 3 hours, which is too long for many applications. The most cost-effective and simplest process is the sol-gel solution followed by facile dip coating to coat the metallic substrates. At the lab scale, it takes approximately 20 minutes to

prepare the sol-gel solution and 30 seconds to coat a 7 cm long tube sample via dip coating. It is worth mentioning that we implemented 30 minutes of 500°C heat treatment in nitrogen atmosphere to improve coating densification but finding the optimal temperature and duration was out of scope of our work. However, we measured the performance of untreated coating and it still showed about 1 order of magnitude higher corrosion resistance compared to the uncoated surface in EIS test. Scalability is another advantage of the sol-gel coating method. The estimated operating expenses and capital expenses for sol-gel coating is \$608/m^2 and \$600, respectively. It should be noted that the sol-gel solution stays fresh for several hours and many samples can be coated with the same solution. At the lab scale, the equipment cost for the Parylene C deposition system is \$60,000 with the maximum sample size of 25 × 25cm, while it is possible to coat an area as large as 0.5 m^2 with sol-gel and superhydrophobic coating methods. The need for a vacuum chamber and high temperature (690°C) to cleave the dimeric Parylene gas to its monomeric form in the Parylene C coating process, makes the scalability to larger heat exchangers difficult and time consuming. On the other hand, sol- gel and superhydrophobic coatings can be applied on very large samples (> 1 m^2) by developing larger dip coating systems for the sol- gel and atmospheric pressure CVD chambers (85°C) for the superhydrophobic coating.

Recently, many studies have shown the anti-corrosion behavior of superhydrophobic surfaces.[54-55] The anti-corrosion behavior of superhydrophobic surfaces is due to the existence of air pockets inside the micro/nanostructures which is representative of the Cassie- Baxter wetting state. However, in order to ensure durable corrosion resistant superhydrophobic surfaces, the stability of the Cassie- Baxter state needs to be considered. At high hydraulic pressures and when there is high vapor condensation on the surface, the stability of Cassie- Baxter is prone to change and the transition to Wenzel state may happen.[56-57] In addition, and just as important, liquid

impalement into the surface structures via high speed droplet impact or jet impingement is another important issue that restricts the exploitation of superhydrophobic surfaces.[58] The risk of transition to the Wenzel state for superhydrophobic surfaces created doubt about their durability for long-term utilization. Although recent studies have shown that sol-gel derived superhydrophobic surfaces have added robustness and durability,[59] more studies are needed on the corrosion resistance performance and degradation mechanism of these coatings at different working conditions. To study the durability and degradation mechanism of the coatings, previous studies have used time-dependent EIS.[60-61] However, no widely accepted approach exists to follow the degradation of the coating-metal system[62] and to exact quantification and decoupling of different parameters such as water uptake, change in the coating dielectric constant, delamination area and pinhole density and size with exposure time.

CHAPTER 9: CONCLUSION

We developed a sol- gel solution and coated Al and Cu substrates with it. Using a facile and controllable dip coating method, we achieved a very smooth (< 5 nm root mean square roughness) coating. Then we compared the anti-corrosion behavior of the sol-gel coating with superhydrophobic, hydrophobic, organic Parylene C, SOCAL and AP MO-CVD of SiO_2 coatings. Hydrophobic surface (fabricated by nanolayer deposition of HTMS) very slightly improved the corrosion resistance of Al and Cu substrates (< 15% protection efficiency in potentiodynamic polarization test). SOCAL did not add any further corrosion resistance to the surfaces. Based on Tafel polarization curves and electrochemical impedance spectroscopy, sol- gel, superhydrophobic and Parylene C coatings showed more than 95% corrosion protection efficiency, with Parylene C showing the best performance. The better performance of the Parylene C is because of the pinhole free coating achieved by using a Specialty Coating Systems Labcoater 2 Parylene deposition system. The analogous result is achieved with AP MO-CVD SiO_2. Lower pinhole density results in a larger charge transfer resistance between the electrolyte and metallic substrate. The corrosion protection of the superhydrophobic coating is because of the existence of air pockets in the structured surface. Comparing the corrosion current as well as the corrosion resistances (e.g. electrochemical impedance spectroscopy measurements) between the superhydrophobic and superhydrophilic surfaces demonstrates the significance of air pockets in inhibiting the corrosion. For a better real-life situation, we built a corrosion flow loop setup and tested the durability and corrosion protection performance of the developed sol-gel, Parylene C and superhydrophobic CuO coatings with sea water passing inside the coated tubes for four days. The sol- gel coated Copper tubes weight loss was 78% smaller at room temperature and 76% smaller at 40°C compared to the uncoated tube. The Parylene C and superhydrophobic CuO coatings showed less than 95% weight

loss compared to the uncoated Cu tubes. SWAAT which is a common method for measuring the corrosion of heat exchanger materials in industry was implemented to better understand the durability and corrosion mechanism of the coatings. After 4 days of SWAAT, all coatings except Parylene C and AP MO-CVD SiO_2 were observed to peel from their respective substrates, showing the importance of coating method in achieving conformal and robust anti-corrosion coatings. Compared to all the investigated coatings, sol-gel was determined to be the most cost-effective and rapid coating. At lab scale, it took less than 30 minutes to develop the solution and coat the samples. Our analysis shows that although Parylene C has the greatest corrosion resistance compared to the tested coatings, it also has the highest potential to degrade heat transfer.

REFERENCES

(1) Abdolah Zadeh, M.; van der Zwaag, S.; Garcia, S. J. Adhesion and Long-Term Barrier Restoration of Intrinsic Self-Healing Hybrid Sol–Gel Coatings. *ACS Applied Materials & Interfaces* **2016,** *8* (6), 4126-4136, DOI: 10.1021/acsami.5b11867.

(2) Obot, I. B.; Meroufel, A.; Onyeachu, I. B.; Alenazi, A.; Sorour, A. A. Corrosion Inhibitors for Acid Cleaning of Desalination Heat Exchangers: Progress, Challenges and Future Perspectives. *Journal of Molecular Liquids* **2019,** *296*, DOI: 10.1016/j.molliq.2019.111760.

(3) Balaji, J.; Roh, S.-H.; Edison, T. N. J. I.; Jung, H.-Y.; Sethuraman, M. G. Sol-Gel Based Hybrid Silane Coatings for Enhanced Corrosion Protection of Copper in Aqueous Sodium Chloride. *Journal of Molecular Liquids* **2020,** *302*, DOI: 10.1016/j.molliq.2020.112551.

(4) Zheludkevich, M. L.; Salvado, I. M.; Ferreira, M. G. S. Sol–Gel Coatings for Corrosion Protection of Metals. *Journal of Materials Chemistry* **2005,** *15* (48), DOI: 10.1039/b419153f.

(5) Yan, W.; Ong, W. K.; Wu, L. Y.; Wijesinghe, S. L. Investigation of Using Sol-Gel Technology for Corrosion Protection Coating Systems Incorporating Colours and Inhibitors. *Coatings* **2019,** *9* (1), 52.

(6) Bera, S.; Rout, T. K.; Udayabhanu, G.; Narayan, R. Comparative Study of Corrosion Protection of Sol–Gel Coatings with Different Organic Functionality on Al-2024 Substrate. *Progress in Organic Coatings* **2015,** *88*, 293-303, DOI: 10.1016/j.porgcoat.2015.07.006.

(7) Cao, X.; Huang, F.; Huang, C.; Liu, J.; Cheng, Y. F. Preparation of Graphene Nanoplate Added Zinc-Rich Epoxy Coatings for Enhanced Sacrificial Anode-Based Corrosion Protection. *Corrosion Science* **2019,** *159*, 108120, DOI: https://doi.org/10.1016/j.corsci.2019.108120.

(8) Syrek-Gerstenkorn, B.; Paul, S.; Davenport, A. J. Sacrificial Thermally Sprayed Aluminium Coatings for Marine Environments: A Review. *Coatings* **2020,** *10* (3), 267.

(9) Talha, M.; Ma, Y.; Xu, M.; Wang, Q.; Lin, Y.; Kong, X. Recent Advancements in Corrosion Protection of Magnesium Alloys by Silane-Based Sol–Gel Coatings. *Industrial & Engineering Chemistry Research* **2020,** *59* (45), 19840-19857, DOI: 10.1021/acs.iecr.0c03368.

(10) Xu, J.; Liu, Y.; Du, W.; Lei, W.; Si, X.; Zhou, T.; Lin, J.; Peng, L. Superhydrophobic Silica Antireflective Coatings with High Transmittance Via One-Step Sol-Gel Process. *Thin Solid Films* **2017,** *631*, 193-199, DOI: https://doi.org/10.1016/j.tsf.2017.03.005.

(11) Boinovich, L. B.; Emelyanenko, A. M.; Modestov, A. D.; Domantovsky, A. G.; Emelyanenko, K. A. Synergistic Effect of Superhydrophobicity and Oxidized Layers on Corrosion Resistance of Aluminum Alloy Surface Textured by Nanosecond Laser Treatment. *ACS Appl Mater Interfaces* **2015,** *7* (34), 19500-8, DOI: 10.1021/acsami.5b06217.

(12) Xiang, T.; Han, Y.; Guo, Z.; Wang, R.; Zheng, S.; Li, S.; Li, C.; Dai, X. Fabrication of Inherent Anticorrosion Superhydrophobic Surfaces on Metals. *ACS Sustainable Chemistry & Engineering* **2018,** *6* (4), 5598-5606, DOI: 10.1021/acssuschemeng.8b00639.

(13) Su, F.; Yao, K. Facile Fabrication of Superhydrophobic Surface with Excellent Mechanical Abrasion and Corrosion Resistance on Copper Substrate by a Novel Method. *ACS Applied Materials & Interfaces* **2014,** *6* (11), 8762-8770, DOI: 10.1021/am501539b.

(14) Quéré, D. Wetting and Roughness. *Annual Review of Materials Research* **2008,** *38* (1), 71-99, DOI: 10.1146/annurev.matsci.38.060407.132434.

(15) Lafuma, A.; Quéré, D. Superhydrophobic States. *Nature Materials* **2003,** *2* (7), 457-460, DOI: 10.1038/nmat924.

(16) Vilaro, I.; Yague, J. L.; Borros, S. Superhydrophobic Copper Surfaces with Anticorrosion Properties Fabricated by Solventless Cvd Methods. *ACS Appl Mater Interfaces* **2017,** *9* (1), 1057-1065, DOI: 10.1021/acsami.6b12119.

(17) Ma, J.; Sett, S.; Cha, H.; Yan, X.; Miljkovic, N. Recent Developments, Challenges, and Pathways to Stable Dropwise Condensation: A Perspective. *Applied Physics Letters* **2020,** *116* (26), 260501, DOI: 10.1063/5.0011642.
(18) Ma, J.; Cha, H.; Kim, M.-K.; Cahill, D. G.; Miljkovic, N. Condensation Induced Delamination of Nanoscale Hydrophobic Films. *Advanced Functional Materials* **2019,** *29* (43), 1905222, DOI: https://doi.org/10.1002/adfm.201905222.
(19) Zucchi, F.; Grassi, V.; Frignani, A.; Trabanelli, G. Inhibition of Copper Corrosion by Silane Coatings. *Corrosion Science* **2004,** *46* (11), 2853-2865, DOI: https://doi.org/10.1016/j.corsci.2004.03.019.
(20) Peng, S.; Zeng, Z.; Zhao, W.; Li, H.; Chen, J.; Han, J.; Wu, X. Novel Functional Hybrid Silica Sol–Gel Coating for Copper Protection Via in Situ Thiol–Ene Click Reaction. *RSC Adv.* **2014,** *4* (30), 15776-15781, DOI: 10.1039/c4ra00142g.
(21) Zhao, H.; Deshpande, C. A.; Li, L.; Yan, X.; Hoque, M. J.; Kuntumalla, G.; Rajagopal, M. C.; Chang, H. C.; Meng, Y.; Sundar, S.; Ferreira, P.; Shao, C.; Salapaka, S.; Sinha, S.; Miljkovic, N. Extreme Antiscaling Performance of Slippery Omniphobic Covalently Attached Liquids. *ACS Applied Materials & Interfaces* **2020,** *12* (10), 12054-12067, DOI: 10.1021/acsami.9b22145.
(22) Yan, X.; Huang, Z.; Sett, S.; Oh, J.; Cha, H.; Li, L.; Feng, L.; Wu, Y.; Zhao, C.; Orejon, D.; Chen, F.; Miljkovic, N. Atmosphere-Mediated Superhydrophobicity of Rationally Designed Micro/Nanostructured Surfaces. *ACS Nano* **2019,** *13* (4), 4160-4173, DOI: 10.1021/acsnano.8b09106.
(23) FitzGerald, K. P.; Nairn, J.; Skennerton, G.; Atrens, A. Atmospheric Corrosion of Copper and the Colour, Structure and Composition of Natural Patinas on Copper. *Corrosion Science* **2006,** *48* (9), 2480-2509, DOI: https://doi.org/10.1016/j.corsci.2005.09.011.
(24) Wang, L.; McCarthy, T. J. Covalently Attached Liquids: Instant Omniphobic Surfaces with Unprecedented Repellency. *Angew Chem Int Ed Engl* **2016,** *55* (1), 244-8, DOI: 10.1002/anie.201509385.
(25) Hoyas, A. M.; Whelan, C. M.; Schuhmacher, J.; Celis, J. P.; Maex, K. Effect of Surface Reactive Site Density and Reactivity on the Growth of Atomic Layer Deposited Wn[Sub X]C[Sub Y] Films. *Electrochemical and Solid-State Letters* **2006,** *9* (7), DOI: 10.1149/1.2203239.
(26) Lemaire, P. C.; King, M.; Parsons, G. N. Understanding Inherent Substrate Selectivity During Atomic Layer Deposition: Effect of Surface Preparation, Hydroxyl Density, and Metal Oxide Composition on Nucleation Mechanisms During Tungsten Ald. *J Chem Phys* **2017,** *146* (5), 052811, DOI: 10.1063/1.4967811.
(27) Boyina, K. S.; Mahvi, A. J.; Chavan, S.; Park, D.; Kumar, K.; Lira, M.; Yu, Y.; Gunay, A. A.; Wang, X.; Miljkovic, N. Condensation Frosting on Meter-Scale Superhydrophobic and Superhydrophilic Heat Exchangers. *International Journal of Heat and Mass Transfer* **2019,** *145*, 118694, DOI: https://doi.org/10.1016/j.ijheatmasstransfer.2019.118694.
(28) Yang, Z.; Wu, Y.-Z.; Ye, Y.-F.; Gong, M.-G.; Xu, X.-L. A Simple Way to Fabricate an Aluminum Sheet with Superhydrophobic and Self-Cleaning Properties. *Chinese Physics B* **2012,** *21* (12), DOI: 10.1088/1674-1056/21/12/126801.
(29) Weisensee, P. B.; Wang, Y.; Qian, H.; Schultz, D.; King, W. P.; Miljkovic, N. Condensate Droplet Size Distribution on Lubricant-Infused Surfaces. *International Journal of Heat and Mass Transfer* **2017,** *109*, 187-199, DOI: https://doi.org/10.1016/j.ijheatmasstransfer.2017.01.119.
(30) Reed, J. H.; Gonsalves, A. E.; Román, J. K.; Oh, J.; Cha, H.; Dana, C. E.; Toc, M.; Hong, S.; Hoffman, J. B.; Andrade, J. E.; Jo, K. D.; Alleyne, M.; Miljkovic, N.; Cropek, D. M.

Ultrascalable Multifunctional Nanoengineered Copper and Aluminum for Antiadhesion and Bactericidal Applications. *ACS Applied Bio Materials* **2019,** *2* (7), 2726-2737, DOI: 10.1021/acsabm.8b00765.
(31) Enright, R.; Miljkovic, N.; Dou, N.; Nam, Y.; Wang, E. N. Condensation on Superhydrophobic Copper Oxide Nanostructures. *Journal of Heat Transfer* **2013,** *135* (9), DOI: 10.1115/1.4024424.
(32) Chou, C.-M.; Shiao, C.-J.; Chung, C.-J.; He, J.-L. Deposition, Characterization, and in Vivo Performance of Parylene Coating on General-Purpose Silicone for Examining Potential Biocompatible Surface Modifications. *Thin Solid Films* **2013,** *549*, 103-107, DOI: https://doi.org/10.1016/j.tsf.2013.09.032.
(33) Surmeneva, M. A.; Vladescu, A.; Cotrut, C. M.; Tyurin, A. I.; Pirozhkova, T. S.; Shuvarin, I. A.; Elkin, B.; Oehr, C.; Surmenev, R. A. Effect of Parylene C Coating on the Antibiocorrosive and Mechanical Properties of Different Magnesium Alloys. *Applied Surface Science* **2018,** *427*, 617-627, DOI: https://doi.org/10.1016/j.apsusc.2017.08.066.
(34) Liu, K.; Vuckovac, M.; Latikka, M.; Huhtamäki, T.; Ras, R. H. A. Improving Surface-Wetting Characterization. *Science* **2019,** *363* (6432), 1147-1148, DOI: 10.1126/science.aav5388.
(35) Nečas, D.; Klapetek, P. Gwyddion: An Open-Source Software for Spm Data Analysis. *Central European Journal of Physics* **2012,** *10* (1), 181-188, DOI: 10.2478/s11534-011-0096-2.
(36) Chauhan, D. S.; Quraishi, M. A.; Carrière, C.; Seyeux, A.; Marcus, P.; Singh, A. Electrochemical, Tof-Sims and Computational Studies of 4-Amino-5-Methyl-4h-1,2,4-Triazole-3-Thiol as a Novel Corrosion Inhibitor for Copper in 3.5% Nacl. *Journal of Molecular Liquids* **2019,** *289*, 111113, DOI: https://doi.org/10.1016/j.molliq.2019.111113.
(37) Gudić, S.; Smoljko, I.; Kliškić, M. The Effect of Small Addition of Tin and Indium on the Corrosion Behavior of Aluminium in Chloride Solution. *Journal of Alloys and Compounds* **2010,** *505* (1), 54-63, DOI: https://doi.org/10.1016/j.jallcom.2010.06.055.
(38) Benítez, J. J.; Heredia-Guerrero, J. A.; San-Miguel, M. A.; Galloway, H. C. Packing Defects in Fatty Amine Self-Assembled Monolayers on Mica as Revealed from Afm Techniques. *The Journal of Physical Chemistry B* **2018,** *122* (2), 493-499, DOI: 10.1021/acs.jpcb.7b03603.
(39) Preiner, M. J.; Melosh, N. A. Identification and Passivation of Defects in Self-Assembled Monolayers. *Langmuir* **2009,** *25* (5), 2585-2587, DOI: 10.1021/la804162a.
(40) Shubha, H. N.; Venkatesha, T. V.; Vathsala, K.; Pavitra, M. K.; Punith Kumar, M. K. Preparation of Self Assembled Sodium Oleate Monolayer on Mild Steel and Its Corrosion Inhibition Behavior in Saline Water. *ACS Applied Materials & Interfaces* **2013,** *5* (21), 10738-10744, DOI: 10.1021/am4028857.
(41) Qi, Y.; Li, X.; He, Y.; Zhang, D.; Ding, J. Mechanism of Acceleration of Iron Corrosion by a Polylactide Coating. *ACS Appl Mater Interfaces* **2019,** *11* (1), 202-218, DOI: 10.1021/acsami.8b17125.
(42) Liu, W.; Zhang, H.; Qu, Z.; Zhang, Y.; Li, J. Corrosion Behavior of the Steel Used as a Huge Storage Tank in Seawater. *Journal of Solid State Electrochemistry* **2010,** *14* (6), 965-973, DOI: 10.1007/s10008-009-0886-2.
(43) Paxson, A. T.; Yagüe, J. L.; Gleason, K. K.; Varanasi, K. K. Stable Dropwise Condensation for Enhancing Heat Transfer Via the Initiated Chemical Vapor Deposition (Icvd) of Grafted Polymer Films. *Advanced Materials* **2014,** *26* (3), 418-423, DOI: https://doi.org/10.1002/adma.201303065.

(44) Yang, G.; Amro, N. A.; Starkewolfe, Z. B.; Liu, G.-y. Molecular-Level Approach to Inhibit Degradations of Alkanethiol Self-Assembled Monolayers in Aqueous Media. *Langmuir* **2004,** *20* (10), 3995-4003, DOI: 10.1021/la0499160.
(45) Hoque, E.; DeRose, J. A.; Houriet, R.; Hoffmann, P.; Mathieu, H. J. Stable Perfluorosilane Self-Assembled Monolayers on Copper Oxide Surfaces: Evidence of Siloxy−Copper Bond Formation. *Chemistry of Materials* **2007,** *19* (4), 798-804, DOI: 10.1021/cm062318h.
(46) Kashchiev, D. *Nucleation*, Elsevier: 2000.
(47) Meijers, S. Corrosion of Aluminum Brazing Sheet. 2002.
(48) Standard Practice for Modified Salt Spray (Fog) Testing.
(49) Zhu, W.; Zheng, G.; Cao, S.; He, H. Thermal Conductivity of Amorphous Sio2 Thin Film: A Molecular Dynamics Study. *Sci Rep* **2018,** *8* (1), 10537, DOI: 10.1038/s41598-018-28925-6.
(50) Callard, S.; Tallarida, G.; Borghesi, A.; Zanotti, L. Thermal Conductivity of Sio2 Films by Scanning Thermal Microscopy. *Journal of Non-Crystalline Solids* **1999,** *245* (1), 203-209, DOI: https://doi.org/10.1016/S0022-3093(98)00863-1.
(51) Hong-seok, N.; Hesketh, P. J.; Frye-Mason, G. C. Parylene Gas Chromatographic Column for Rapid Thermal Cycling. *Journal of Microelectromechanical Systems* **2002,** *11* (6), 718-725, DOI: 10.1109/JMEMS.2002.805052.
(52) Para Coat Technologies Inc. Parylene C Technical Data Sheet. https://pctconformalcoating.com/parylene/parylene-thermal-properties/ (accessed 29 April).
(53) Petukhov, B. In *Proceedings of the 1961-62 Heat Transfer Conference*, 1962.
(54) Li, H.; Yu, S.; Hu, J.; Yin, X. Modifier-Free Fabrication of Durable Superhydrophobic Electrodeposited Cu-Zn Coating on Steel Substrate with Self-Cleaning, Anti-Corrosion and Anti-Scaling Properties. *Applied Surface Science* **2019,** *481*, 872-882, DOI: https://doi.org/10.1016/j.apsusc.2019.03.123.
(55) Yao, W.; Liang, W.; Huang, G.; Jiang, B.; Atrens, A.; Pan, F. Superhydrophobic Coatings for Corrosion Protection of Magnesium Alloys. *Journal of Materials Science & Technology* **2020,** *52*, 100-118, DOI: https://doi.org/10.1016/j.jmst.2020.02.055.
(56) Chen, R.; Jiao, L.; Zhu, X.; Liao, Q.; Ye, D.; Zhang, B.; Li, W.; Lei, Y.; Li, D. Cassie-to-Wenzel Transition of Droplet on the Superhydrophobic Surface Caused by Light Induced Evaporation. *Applied Thermal Engineering* **2018,** *144*, 945-959, DOI: https://doi.org/10.1016/j.applthermaleng.2018.09.011.
(57) Wier, K. A.; McCarthy, T. J. Condensation on Ultrahydrophobic Surfaces and Its Effect on Droplet Mobility: Ultrahydrophobic Surfaces Are Not Always Water Repellant. *Langmuir* **2006,** *22* (6), 2433-2436, DOI: 10.1021/la0525877.
(58) Peng, C.; Chen, Z.; Tiwari, M. K. All-Organic Superhydrophobic Coatings with Mechanochemical Robustness and Liquid Impalement Resistance. *Nat Mater* **2018,** *17* (4), 355-360, DOI: 10.1038/s41563-018-0044-2.
(59) Dyett, B. P.; Wu, A. H.; Lamb, R. N. Toward Superhydrophobic and Durable Coatings: Effect of Needle Vs Crater Surface Architecture. *ACS Applied Materials & Interfaces* **2014,** *6* (12), 9503-9507, DOI: 10.1021/am501900b.
(60) Zhang, Y.; Feyerabend, F.; Tang, S.; Hu, J.; Lu, X.; Blawert, C.; Lin, T. A Study of Degradation Resistance and Cytocompatibility of Super-Hydrophobic Coating on Magnesium. *Materials Science and Engineering: C* **2017,** *78*, 405-412, DOI: https://doi.org/10.1016/j.msec.2017.04.057.

(61) Mansfeld, F. Use of Electrochemical Impedance Spectroscopy for the Study of Corrosion Protection by Polymer Coatings. *Journal of Applied Electrochemistry* **1995,** *25* (3), 187-202, DOI: 10.1007/BF00262955.
(62) Fan, C.; Shi, J.; Dilger, K. Water Uptake and Interfacial Delamination of an Epoxy-Coated Galvanized Steel: An Electrochemical Impedance Spectroscopic Study. *Progress in Organic Coatings* **2019,** *137*, 105333, DOI: https://doi.org/10.1016/j.porgcoat.2019.105333.